

New physical effects induced by the PZT layer integrated in AlGaN/GaN HEMTs

by

Wei Zhao

A Thesis Submitted to The University of Twente

in Partial Fulfillment of the Requirements for

the Degree of Master of Science

in the Faculty of

Electrical Engineering, Mathematics and Computer Science

Major: Electrical Engineering

Examination committee:

Dr.ir. R.J.E. Hueting

Prof.dr. D.J. Gravesteijn

Prof.dr.ir. G. Koster

July 2018

Abstract

The successful high quality epitaxial growth of a lead zirconate titanate (PZT) thin film on GaN offered available experimental samples for this research, where the physical effects of the PZT layer integrated in AlGaIn/GaN HEMTs were investigated. Device simulation results indicate that the two-dimensional electron gas (2DEG) density at the AlGaIn/GaN interface scales linearly with the polarization of PZT. It has been found how the permittivity of PZT influences the breakdown voltage depends on whether PZT is regarded as an insulator or semiconductor.

PZT has been confirmed to be conducting by $I - V$ measurements. A deviation was observed between the two $I - V$ curves within a dual sweep, which can be related the difference of PZT polarization in the two opposite sweep directions. Devices with 0.52 Zr composition exhibited the largest reduction of on-resistance (R_{on}) when the gate voltage was increased from -1.5 V to 0 V. This can be explained by the largest difference between remnant polarization (P_r) and saturation polarization (P_s) of PZT with 0.52 Zr composition. Devices with 0.52 Zr composition also showed the highest gate leakage, which can be explained by the hole induced gate leakage proposed in this thesis. Breakdown measurements appeared to show some improvement in our HEMTs compared to conventional counterparts reported in the literature, though more dedicated test structures are needed to analyze these more carefully.

Keywords: Ferroelectrics, HEMT, PZT, polarization, power, composition.

Acknowledgements

I am incredibly grateful to my supervisor Dr.ir. R.J.E. Hueting for his constant guidance and inspirations through my thesis. He introduced me into the challenging and exciting field of GaN HEMTs, gave me instructions on Silvaco Atlas for simulation, showed me an analytical mind to solve complex problems, helped me with laboratory work, provided regular feedbacks and discussions about the results, as well as revised my thesis drafts. I would like to thank Prof.dr. D.J. Gravesteijn, who arranged meetings with me once every two weeks to discuss my progress and offer suggestions. In addition, I also want to express my gratitude to T. Schut who did the wire bonding for me. His help was an essential step of the breakdown voltage measurement. I would also like to thank Prof.dr. J. Schmitz, Hendrikus de Vries, and Thomas Hoen for advice on building and connecting measurement instruments.

My special thanks go to Dr. L. Li and Prof.dr.ir. G. Koster from the IMS group for their PZT-on-GaN HEMT devices. Without their samples, this thesis would have been impossible!

Table of Contents

ABSTRACT	I
ACKNOWLEDGEMENTS.....	II
TABLE OF CONTENTS.....	III
1 INTRODUCTION	1
1.1 Motivation.....	1
1.2 Objectives	2
1.3 Methodology.....	3
1.4 Outline of this thesis	3
2 LITERATURE SURVEY.....	5
2.1 Fundamentals of high electron mobility transistors	5
2.2 AlGaIn/GaN HEMTs.....	6
2.3 PZT	9
3 EXPERIMENTAL.....	13
3.1 Process details.....	13
3.2 Device specifications	13
3.3 Measurement setup	15
4 TCAD SIMULATIONS.....	17
4.1 Model construction	17
4.2 I-V characterization.....	20
4.3 Band diagram and 2DEG density.....	21
4.4 On-resistance and threshold voltage	23
4.5 Subthreshold swing.....	24
4.6 Breakdown voltage	25
5 ELECTRICAL CHARACTERIZATION	31

5.1	Devices functionality check	31
5.2	Output characteristics.....	33
5.3	Transfer characteristics	37
5.4	Off-state breakdown.....	43
5.5	Summary	46
6	CONCLUSIONS AND RECOMMENDATIONS.....	48
6.1	Conclusions.....	48
6.2	Recommendations.....	49
	REFERENCES	51
	APPENDIX	57

1 Introduction

1.1 Motivation

Power electronics offer a wide range of applications ranging from power supply systems to motor vehicle drives, fuel cell converters, inverters, and high-frequency heating. The market as a whole was about \$20 billion in 2012, and power electronics will remain one of the most attractive branches of the semiconductor industry over the next decade [1]. As in most other electronics areas, silicon also has been the predominant semiconductor in power electronics to date [2]. However, wide bandgap materials like gallium-nitride (GaN) has received significant research interest due to its unique material properties including a wide energy bandgap and high electron mobility, which enable the operation of electron devices at higher voltages and large energy savings compared to silicon counterparts. Consequently, GaN-based high-electron mobility transistors (HEMTs) featured with a two-dimensional electron gas (2DEG) are emerging as promising candidates for high voltage, high power and high frequency applications.

Intensive investigations have been carried out on GaN-based HEMTs and significant progress has been made. Recently the integration of lead zirconate titanate ($\text{PbZr}_x\text{Ti}_{1-x}\text{O}_3$ or PZT) with GaN has attracted the attention in the scientific community, because of its ferroelectric properties such as a large remnant polarization and a large dielectric constant. However, the large lattice mismatch between PZT and GaN makes the epitaxial growth of PZT on GaN challenging [3]. Promisingly, high quality epitaxial growth of a PZT thin film on an AlGaN/GaN HEMT has been achieved by Dr. L. Li *et al.* from the inorganic material science (IMS) group of University of Twente, utilizing MgO as a buffer layer to overcome the lattice mismatch [4]. The schematic

cross-section of such a PZT-on-GaN¹ HEMT is shown in Fig. 1.1. Their work offers an opportunity to investigate the interesting physical effects from such a PZT layer.

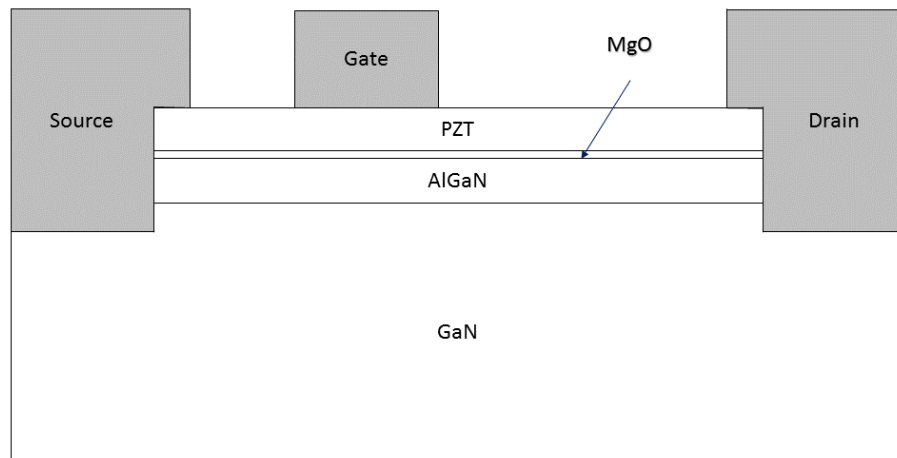


Fig. 1.1. A schematic cross-section view of a PZT-on-GaN HEMT fabricated by the IMS group of University of Twente. The MgO layer was utilized as a buffer layer to overcome the lattice mismatch between AlGaN and PZT.

1.2 Objectives

Since the epitaxial growth of PZT on an AlGaN/GaN HEMT has been challenging until the achievement of the IMS group. Few research regarding this field have been initiated. The PZT layer could have an influence on the output characteristics, transfer characteristics, and off-state breakdown characteristic. For example, the large dielectric constant of PZT might be helpful to increase the breakdown voltage (BV), which is an advantage in the high power application. If the

¹ In a real device, there is another GaN buffer layer between PZT and AlGaN. This is why the devices are called “PZT-on-GaN” HEMTs. This GaN layer is in principle not important for the general functioning of the HEMT, but for the passivation and contacting. For simplicity, such GaN layer is not shown in Fig. 1.1.

polarization of PZT can increase the 2DEG density, then a decreased on-resistance (R_{on}) can be expected, which is desirable because the energy dissipation can be reduced accordingly. On the contrary, if R_{on} is increased, the integration of PZT could be a disadvantage. In addition, it has not been confirmed whether PZT behaves like an insulator or semiconductor after it is integrated in an HEMT, nor is it clear whether it can break down. Therefore, the objective of this research is to investigate the physical effects from the PZT layer integrated on an AlGaIn/GaN HEMT.

Main research questions include:

- (1) Does PZT act like an insulator or semiconductor in a PZT-on-GaN HEMT?
- (2) What is the effect of PZT on the on-state behavior, *e.g.*, on-state currents, on-resistance, threshold voltage, and gate leakage?
- (3) What is the effect of PZT on the breakdown voltage?
- (4) How does the Zr composition of PZT influence the characteristics mentioned above?

1.3 Methodology

The research methodology includes a literature survey, technology computer aided design (TCAD) simulations using Silvaco Atlas, DC electrical characterization using the Keithley instruments, and data processing and analysis by Matlab.

1.4 Outline of this thesis

This thesis first provides an introduction to the topic, including the background, motivation, objectives, and methodology (already discussed above in Chapter 0). The following contents start with Chapter 2, a literature survey on the technology of HEMT and the properties of PZT. It is followed by Chapter 3, a description of the process details and specifications of the samples measured in this thesis, as well as the measurement setup. Chapter 4 discusses the TCAD simula-

tion, followed by Chapter 5 where the electrical characterization results and discussions are presented. The thesis ends with Chapter 6, the conclusions with several recommendations for the future research. The simulation script can be found in Appendix.

2 Literature survey

2.1 Fundamentals of high electron mobility transistors

The first HEMT device was reported in 1980 [5], based on the aluminium-gallium-arsenide/gallium-arsenide (AlGaAs/GaAs) heterostructure. Due to the fact that AlGaAs has a lower electron affinity, hence higher conduction band than GaAs, there is a conduction band offset between the two semiconductor layers. As a result, a potential well is formed at the hetero-interface and the electrons are confined in this potential well, which is known as two-dimensional electron gas (2DEG). The cross-section of the structure and the band diagram are shown in Fig. 2.1 [6]. Such devices are typically used for high frequency applications, such as for mobile communication. However, for high-voltage (power) devices used for dc-dc conversion for instance wide bandgap materials such as gallium-nitride (GaN) are interesting.

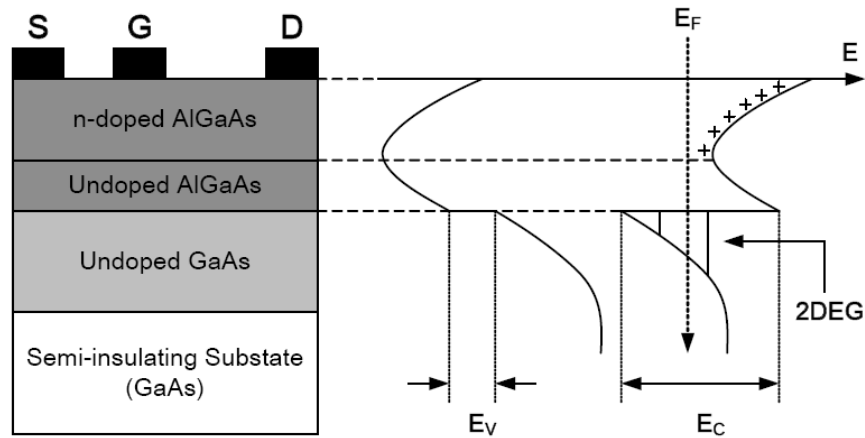


Fig. 2.1. Schematic structure of an AlGaAs/GaAs HEMT and the corresponding energy band diagram [6].

Properties of semiconductor materials relevant to power devices include the bandgap (E_g), critical field strength (E_c), carrier mobility (μ) and thermal conductivity [7]. The maximum voltage that can be supported by a power device before the onset of significant current flow is called

the breakdown voltage (BV), which is governed by the avalanche breakdown phenomenon. Avalanche breakdown typically occurs when the electric field within any local region of a power device approaches E_c [8]. Consequently, in order to obtain a high BV , a high E_c is needed. The relationship between E_c and E_g has been derived by means of a least square method for direct-gap semiconductors, which can be described by [9]:

$$E_c = 2.38 \times 10^5 E_g^{2.5}. \quad (2.1)$$

Ideally, HEMTs are desired to have a high breakdown voltage and low on-state resistance (R_{on}), but they cannot be achieved at the same time. The tradeoff between BV and the specific on-state resistance $R_{on,sp}$ is given by Equation (2.2) [10]

$$R_{on,sp} = \frac{BV^2}{q\mu Q_s E_c^2} \quad (2.2)$$

where q is the elementary charge and Q_s is 2DEG density.

2.2 AlGaIn/GaN HEMTs

Compared to GaAs with a bandgap of 1.43 eV, GaN has a wider bandgap of 3.4 eV and thus a higher critical electric field, of which the typical value is 3.3 MV/cm (330 V/ μ m) [11]. Therefore GaN-based HEMTs have an advantage over GaAs-based ones for high voltage applications. Moreover, III-N materials also exhibit strong spontaneous polarization and piezoelectric effects, which lead to a higher 2DEG density compared to similar 2DEGs in an AlGaAs/GaAs heterostructure.

GaN as well as AlGaIn has a wurtzite crystal structure. The orientation of the GaN crystal can be Ga-faced or N-faced, as shown in Fig. 2.2 [12]. Because of the intrinsic asymmetry in the III-N wurtzite lattice, dipoles are formed which result in both spontaneous and piezoelectric polarization. It has been found empirically that the orientation of high-quality nitride films grown by

metalorganic chemical vapor deposition (MOCVD) is typically Ga-faced. The spontaneous polarization (\mathbf{P}_{sp}) of GaN and AlGaN was found to be pointing from Ga-face to N-face [13], meaning that for Ga-faced AlGaN/GaN heterostructures the spontaneous polarization is negative, as shown in Fig. 2.3 [14]. Both experimental [15] and theoretical [13] results have indicated that the piezoelectric polarization (\mathbf{P}_{pz}) is negative for tensile and positive for compressive strained barriers, respectively. Since GaN has a larger lattice constant than AlGaN, the AlGaN layer grown on the GaN layer is tensile, and accordingly \mathbf{P}_{sp} is parallel to \mathbf{P}_{pz} for AlGaN barrier, as shown in Fig. 2.3.

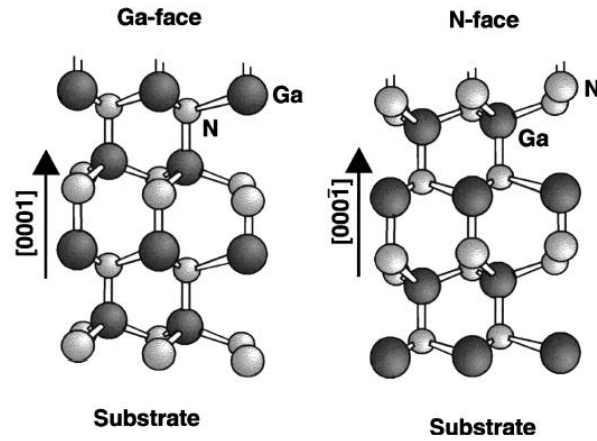


Fig. 2.2. Schematic drawing of the crystal structure of wurtzite Ga-face and N-face GaN [12].

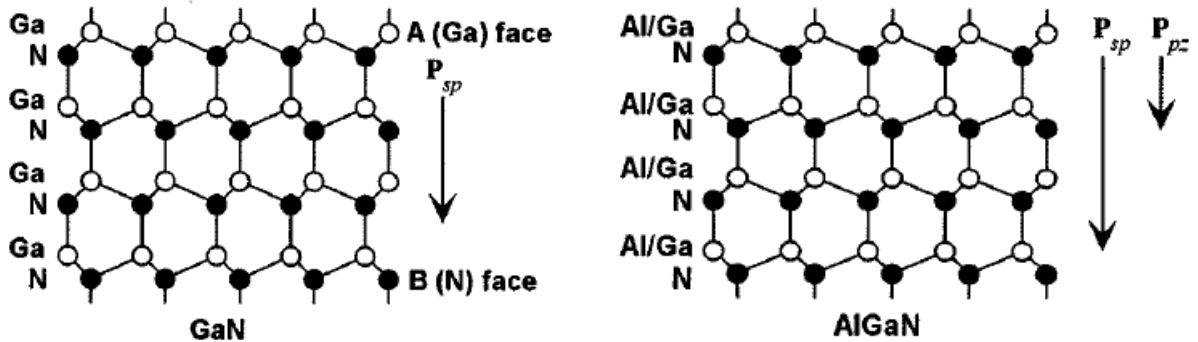


Fig. 2.3. Direction of spontaneous polarization (\mathbf{P}_{sp}) and piezoelectric polarization (\mathbf{P}_{pz}) for GaN (left) and for AlGaN (right) [14].

Therefore, besides the conduction band offset between GaN and AlGaN, \mathbf{P}_{sp} and \mathbf{P}_{pz} are also involved in the formation of the 2DEG. The polarization effect of the AlGaN layer grown on a GaN buffer induces positive polarization charges in the AlGaN layer at the AlGaN/GaN interface, and negative polarization charges at the top of AlGaN layer. Thus a polarization induced built-in electric field is formed. Consequently the energy band of AlGaN is tilted and electrons will move towards the location with lower energy. The process is demonstrated in Fig. 2.4 [16]. When contacting the GaN layer, the electrons will flow into the GaN side and accumulate at the interface.

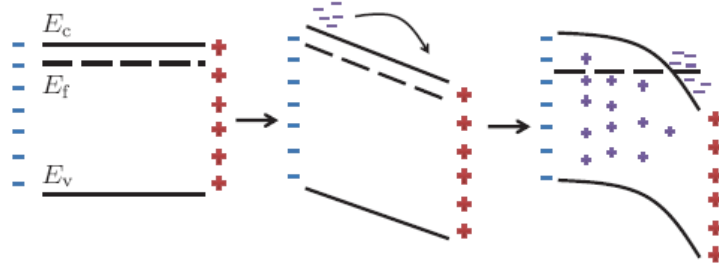


Fig. 2.4. Energy band of AlGaN which is tilted due the polarization induced electric field. The electrons then move to the lower energy position [16].

The total polarization-induced sheet charge at the AlGaN/GaN interface is given by [17]

$$\sigma_{\pi}(x) = \Delta P_{sp}(x) + 2 \left(e_{31}(x) - e_{33}(x) \frac{c_{13}(x)}{c_{33}(x)} \right) \times \left(\frac{a(x) - a_{GaN}}{a_{GaN}} \right) \quad (2.3)$$

where x is the aluminum composition of the alloy, $e_{31}(x)$, $e_{33}(x)$, $c_{13}(x)$, and $c_{33}(x)$ are the relevant piezoelectric and elastic constants for $\text{Al}_x\text{Ga}_{1-x}\text{N}$, $\Delta P_{sp}(x)$ is the difference in spontaneous polarization of the AlGaN barrier and GaN buffer, and $a(x)$, a_{GaN} are the lattice constants of $\text{Al}_x\text{Ga}_{1-x}\text{N}$ and GaN respectively. The 2DEG density n_{2d} can be calculated by the charge control

model [17]. The calculation result suggests n_{2d} depends on Al composition x as well as the barrier layer thickness t_b , as shown in Fig. 2.5 [17]. As the barrier thickness is increased, n_{2d} increases and gradually approaches $\sigma_\pi(x)$. Higher Al composition results in larger $\sigma_\pi(x)$ and larger n_{2d} , and n_{2d} can easily reach $10^{13}/\text{cm}^2$. Typically the 2DEG density for GaN based HEMTs is several times higher than that for GaAs based ones [18].

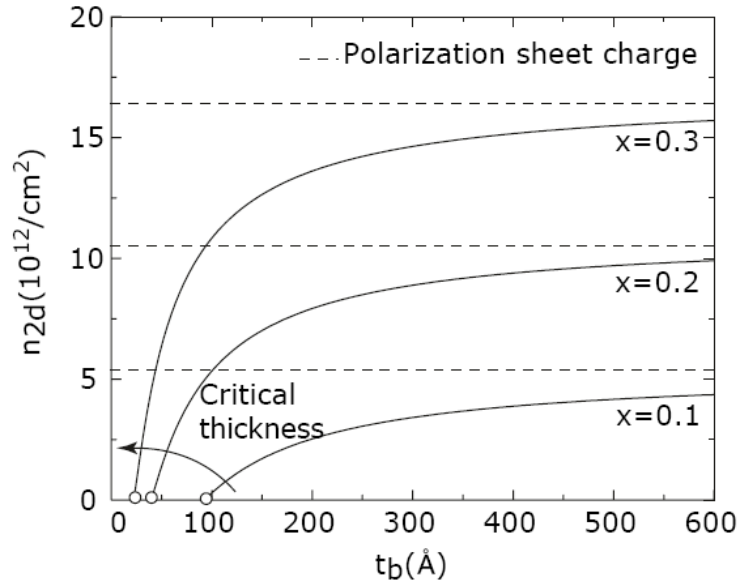


Fig. 2.5. The dependency of 2DEG density on Al composition x and the barrier layer thickness t_b . As the barrier thickness is increased, the 2DEG density gradually approaches the polarization sheet charge density $\sigma_\pi(x)$ [17].

2.3 PZT

Lead zirconate titanate $\text{PbZr}_x\text{Ti}_{1-x}\text{O}_3$ ² (abbreviated as PZT) is a solid solution of PbZrO_3 and PbTiO_3 compounds. It has an ABO_3 type perovskite structure where A is a metal ion with a +2

² Previously x has been used to represent the aluminum composition in AlGaN. Considering the fact that it is not convenient to adopt another symbol, thus x is also used for the composition of Zr. Readers can easily tell its meaning according to the context.

valence (*e.g.*, Pb) and B is a metal ion with a +4 valence (*e.g.*, Ti, Zr). The crystal structure is shown in Fig. 2.6 [19]. Below the Curie temperature (T_C), PZT exhibits superior ferroelectric properties such as high remnant polarization (P_r) [20], high dielectric constants ϵ_r and low coercive field³ [21].

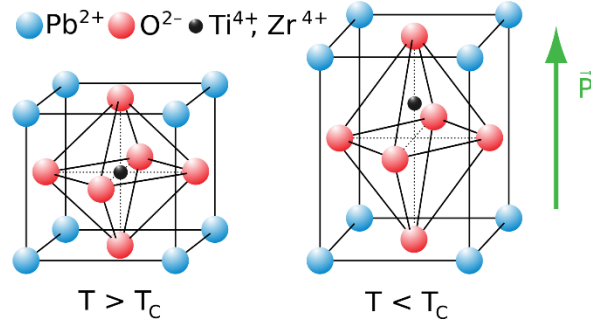


Fig. 2.6. Perovskite structure of PZT [19].

The properties of $PbZr_xTi_{1-x}O_3$ depend on the Zr composition and temperature, according to a $PbTiO_3$ - $PbZrO_3$ phase diagram [22]. The diagram indicates that there is a morphotropic phase boundary (MPB) in the $PbTiO_3$ - $PbZrO_3$ system at a Zr/Ti ratio of about 52/48. The remnant polarization (P_r), saturation polarization (P_s), and relative permittivity (ϵ_r) are enhanced near the MPB. It was revealed that these properties also depend on the orientation of PZT films, as shown in Fig. 2.7 [23]. The thickness of the PZT ranged from 200 nm to 300 nm, and the measurements were conducted in the vertical direction, *i.e.*, along the direction of the PZT thin film growth. It can be seen from Fig. 2.7 that both P_r and P_s of $\{111\}$ -oriented films peak near the MPB composition. The coercive field of PZT with $x = 0.52$ was reported to be 40 kV/cm

³ Conventionally the coercive field is represented by the symbol E_c , which is in conflict with the critical field. To avoid misunderstanding, it is clarified that E_c refers to the critical field in this report. In the situation where coercive field is referenced, its full name will be used instead of the symbol.

[23]. The polarization-electric field ($P - E$) loop of $\text{PbZr}_{0.52}\text{Ti}_{0.48}\text{O}_3$ was measured by Dr. L. Li as well, but in the lateral direction, as shown in Fig. 2.8 [4]. Extracted from the $P - E$ loop in Fig. 2.8, P_r is around $20 \mu\text{C}/\text{cm}^2$, P_s is around $36 \mu\text{C}/\text{cm}^2$, and the coercive field is around 26 kV/cm.

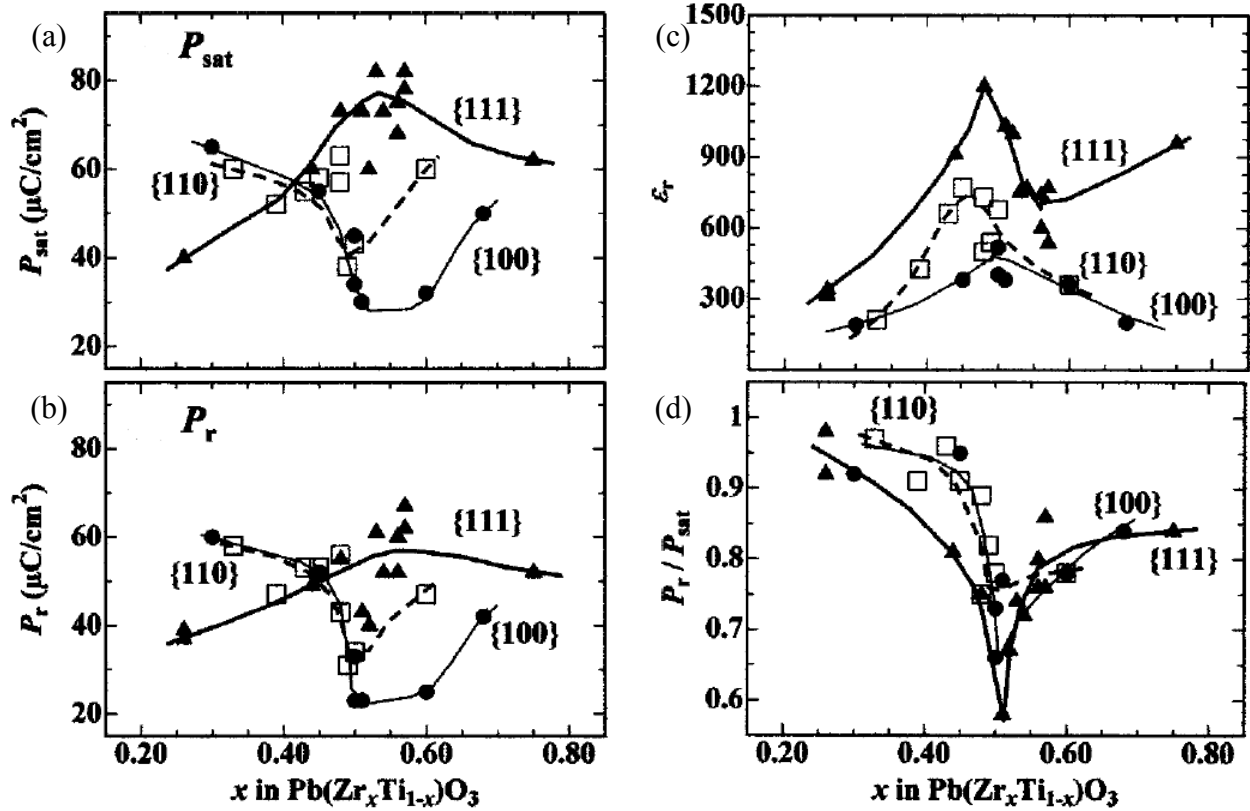


Fig. 2.7. Saturation polarization P_s (a), remnant polarization P_r (b), relative permittivity ϵ_r (c), and the ratio of P_r to P_s (d) as functions of PZT thin film composition and orientation [23]. The measurements were in the vertical direction, *i.e.*, along the direction of the PZT thin film growth.

By comparing Fig. 2.7 with Fig. 2.8, it can be found that the polarization values in the vertical direction is different from that of the lateral direction, which implies that PZT is strongly anisotropic. The ferroelectric perovskites are traditionally considered insulating materials mostly due to the ionic nature of the chemical bonds. Nevertheless, PZT has been revealed to behave like a

p-type semiconductor with standard Schottky contacts with metals [24]. Therefore it would might bring interesting effects when integrated in an HEMT.

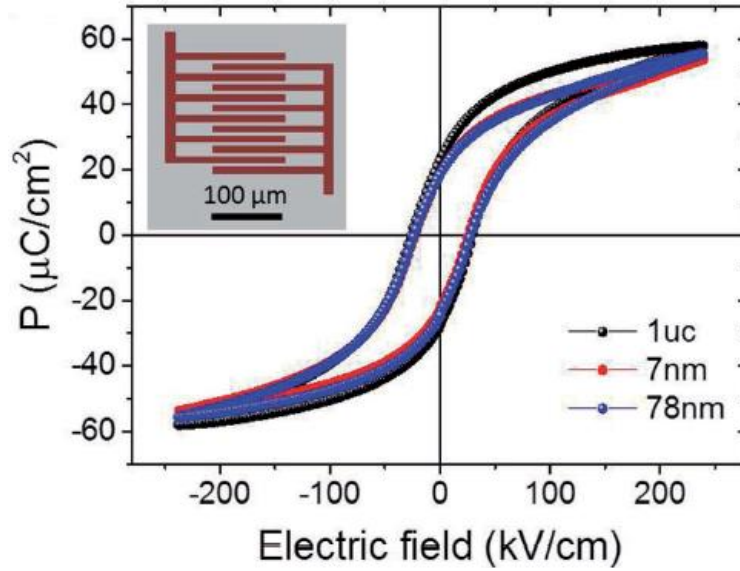


Fig. 2.8. Hysteresis loop of $\text{PbZr}_{0.52}\text{Ti}_{0.48}\text{O}_3$ measured in the lateral direction by Dr. L. Li from the IMS group [4]. Extracted from the $P - E$ loop, P_r is around $20 \mu\text{C}/\text{cm}^2$, P_s is around $36 \mu\text{C}/\text{cm}^2$, and the coercive field is around $26 \text{kV}/\text{cm}$.

3 Experimental

3.1 Process details

The PZT-integrated HEMT samples investigated in this research were provided by the IMS group of University of Twente. An MgO layer was used as a buffer layer in order to achieve epitaxial growth of PZT on a AlGa_xN/GaN HEMT structure [4]. The pulsed laser deposition (PLD) technique was utilized to produce strain free epitaxy of a monolayer MgO ultrathin buffer layer on AlGa_xN/GaN, and then the subsequent epitaxial growth of PZT thin film. The crystal orientation of GaN, MgO and PZT were observed to be (0001), (111) and (111) respectively. Furthermore, the lattice constants of the PZT films was found to be identical to the bulk PZT, which indicated that the PZT films grown on MgO were stress free [4]. The metals used for electrodes were Al/Ti for source and drain while Au/Ti for gate.

3.2 Device specifications

A single HEMT sample is referred to as “device” in this report. The following parameters are the same for all devices. The Al composition of Al_xGa_{1-x}N is 0.2. The thickness is 20 nm for AlGa_xN and 1500 nm for GaN. The length of gate L_g was fixed to 2 μ m. The gate width (W) is 30 μ m. The devices vary in Zr composition of PbZr_xTi_{1-x}O₃, source-drain spacing (L_{sg}), gate-drain spacing (L_{gd}) and the overlap between electrodes (source and drain) and PZT. There are three different Zr/Ti ratios (*i.e.*, three Zr compositions) in total, which are 20/80, 52/48 and 80/20 ($x = 0.2, 0.52$ and 0.80 respectively). The devices with same Zr composition are fabricated on one chip, with each chip assigned a unique label. The investigated samples including corresponding Zr/Ti ratios are summarized in Table 3-1. The chip with Zr/Ti ratio of 52/48 is shown as an example in Fig. 3.1 (a).

Table 3-1 Summary of the investigated samples including chip labels and Zr/Ti ratios

Chip Label	Zr/Ti ratio	PZT thickness
08282016-1	20/80	100 nm
08262016-3	52/48	50 nm
08282016-4	80/20	100 nm

Each chip contains devices with L_{gd} ranging from $2 \mu\text{m}$ to $9 \mu\text{m}$ and L_{sg} ranging from $1.5 \mu\text{m}$ to $3 \mu\text{m}$. All three chips have the identical layout of devices, as shown in Fig. 3.1 (b). Each device is labelled with three numbers separated by dash lines, which indicate the source-gate spacing, gate-drain spacing and metal-PZT overlap, respectively. For instance, the device label “2-3-1” means that $L_{sg} = 2 \mu\text{m}$, $L_{gd} = 3 \mu\text{m}$ and the overlap is $1 \mu\text{m}$.

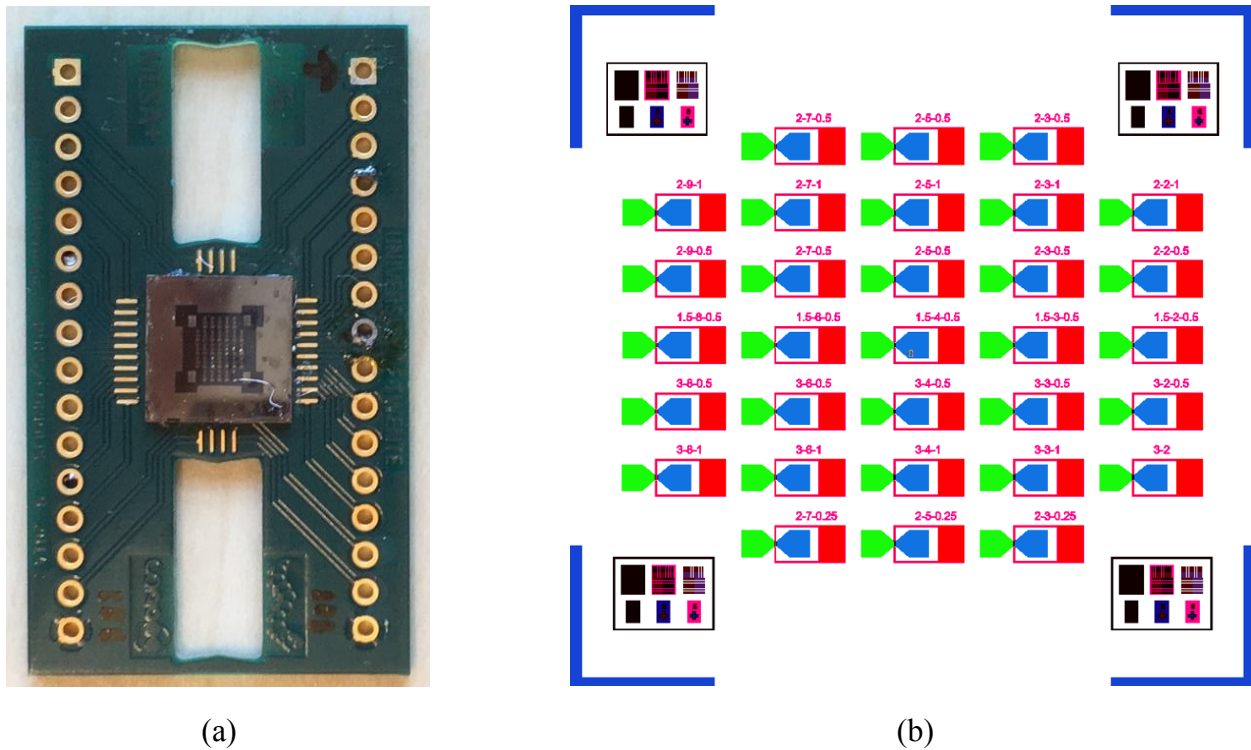


Fig. 3.1. The photo of the chip on a PCB (a). The mask layout of the devices on the chip (b). The chip and its layout was provided by the IMS group (Dr. L. Li, Prof. G. Koster). The bonding was done by T. Schut, with courtesy.

3.3 Measurement setup

3.3.1 On-state measurements

The on-state measurements were performed on the PM 300 probe station with Keithley 4200-SCS, as shown in Fig. 3.2 (a). For $I_d - V_{ds}$ measurements, the source voltage (V_s) was fixed to 0 V and the drain voltage (V_d) was swept from 0 V to 6 V and then back to 0 V (dual sweep) with a step of 0.05 V, when the gate voltage (V_g) was set to -2 V, -1.5 V, -1 V, -0.5 V, and 0 V, respectively. For $I_d - V_{gs}$ measurements, the source voltage (V_s) was fixed to 0 V and the gate voltage (V_g) was swept from -5 V to 5 V and then back to -5 V (dual sweep) with a step of 0.1 V, when the drain voltage (V_d) was set to 0.25 V and 1 V, respectively.



Fig. 3.2. The photo of PM 300 probe station (a), Keithley 8010 (b) on the top, and Keithley 2657A (b) at the bottom.

3.3.2 Off-state breakdown measurements

The maximum voltage supply of Keithley 4200-SCS is 210 V, which was expected to be not sufficient to measure the breakdown voltage in our HEMTs. Thus it was substituted by the

Keithley 2657A model, a high power system source meter, as shown in Fig. 3.2 (b) at the bottom. Besides, for safety precautions, the probe station had to be replaced by the Keithley 8010 model, which provides a safe, low noise, and complete environment for high voltage measurements, as shown in Fig. 3.2 (b) on top. When the lid of Keithley 8010 is lifted, the power supply will be automatically cut off to ensure safety. Moreover, another source meter was needed to supply a voltage to the gate for a three-terminal breakdown measurement.

However, unlike a probe station where the needles are to be positioned on the bond pads of the devices, the measurement with the Keithley 8010 is much more complicated. The chip had to be first glued on a PCB, and then the bond pads of the devices on the chip had to be connected to the narrow metal stripes through wire bonding (thin Al line), as shown in Fig. 3.1 (a). The next step was to solder one end of a wire to a hole on the PCB, according to the PCB layout. The final step was to connect the other end of the wire to an electrode on the Keithley 8010 test board. Obviously, three times of wire bonding and soldering are required for the three-terminal breakdown measurement of each device. Considering the fact that the bonded wires are fragile and that the breakdown could occur between the wires if they are too dense, solely the breakdown voltage of the gate-drain diode was measured instead of the three-terminal measurement.

The Keithley 8010 was connected to the Keithley 2657A, and a communication link was built between Keithley 2657A and a computer. The test script builder (TSB) was used to program the instrument and perform the measurements automatically. The gate potential V_g was set to 0 V and drain potential V_d was swept from 0 V to 1500 V with a step of 0.5 V. The current limit was set to 300 μA and the measurement would stop if it was reached.

4 TCAD simulations

The purpose of the simulations is to investigate the physical effects induced by the PZT layer grown on GaN in an AlGaIn/GaN HEMT and provide explanations to the observed effects from experiments. The technology computer aided design (TCAD) software used for simulations was the two-dimensional (2-D) device simulation tool Silvaco Atlas, version 5.21.3.C. The characterization parameters investigated include the 2DEG density, on-state resistance (R_{on}), threshold voltage (V_{th}), and breakdown voltage (BV).

4.1 Model construction

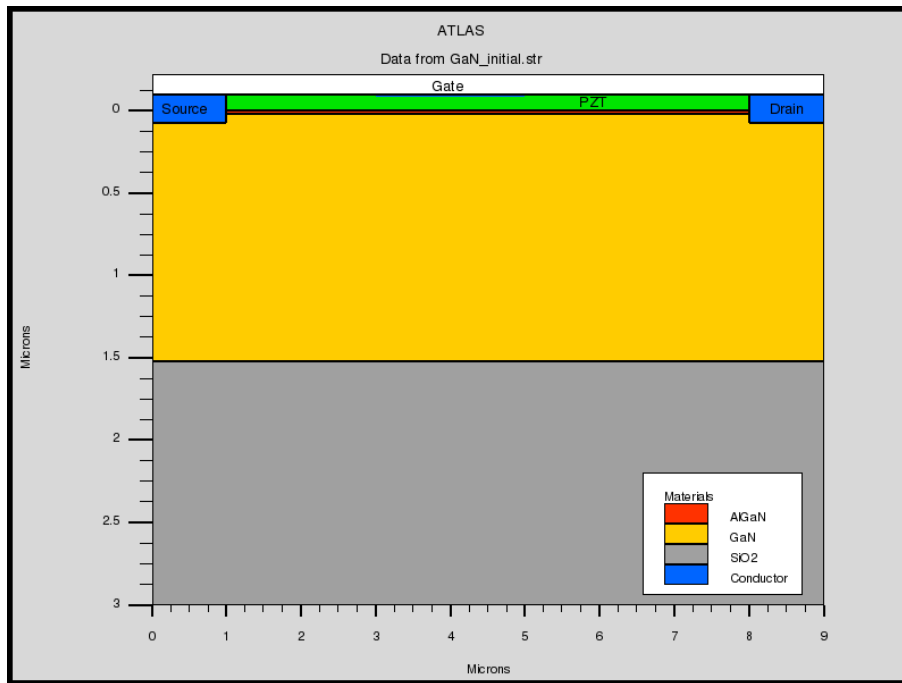


Fig. 4.1. The cross-section of the simulated devices.

The physical model of the simulated device was based on the real geometric size of the sample “2-3-1” as mentioned in Chapter 3.2. The cross-section of the simulated device is shown in Fig. 4.1, where $L_{sg} = 2 \mu\text{m}$ and $L_{gd} = 3 \mu\text{m}$. The thickness of PZT layer was set to 100 nm and the

width of source and drain was $1 \mu\text{m}$. The vertical spacing of the mesh lines is 4 nm near the PZT/AlGa N interface and 0.4 nm near the AlGa N /Ga N interface. The horizontal spacing of the mesh lines is $0.1 \mu\text{m}$. These geometric parameters above apply to all simulations discussed in this report unless stated otherwise. To reduce the complexity of the physical model, several simplifications were adopted. The overlap of source/drain with PZT was ignored. The MgO layer was not added between PZT and AlGa N . The gate was designed as a planar electrode. Thus in this report such simplifications are assumed not to fundamentally affect the simulation results.

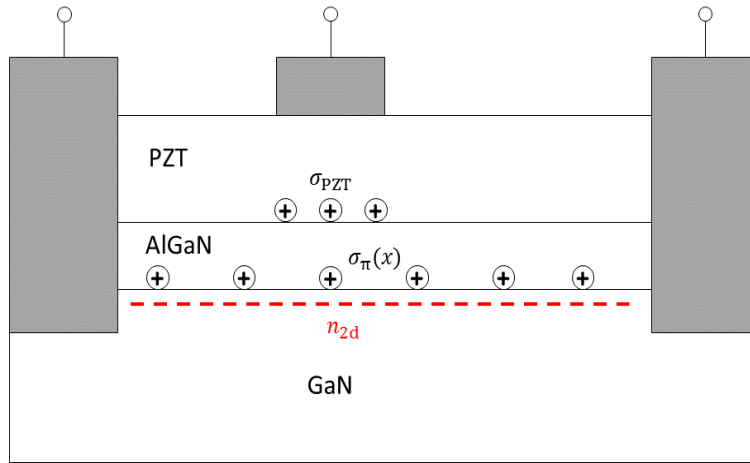


Fig. 4.2. Illustration of σ_{PZT} and $\sigma_{\pi}(x)$ of the simulated device.

The material of PZT was not found in the Silvaco library, thus it was substituted by a semiconductor (germanium)⁴, with relevant parameters modified in the “material” statement in the simulation script to match the parameters of PZT. Despite the ferroelectric properties of PZT, for con-

⁴ In the early stage of the simulation PZT was substituted by nitride. Later on both measurements and related literature indicated that PZT behaves like a semiconductor. Therefore in the final stage of the simulations germanium was adopted as the material for PZT in most cases.

venience sake its physical parameters (remnant) polarization and relative permittivity were considered to be constant. To simulate the total polarization sheet charge $\sigma_{\pi}(x)$ at the AlGaN/GaN heterostructure, an interface charge of $1.05 \times 10^{13} \text{ cm}^{-2}$ was added at the AlGaN/GaN interface. The value of $\sigma_{\pi}(x)$ was taken from Fig. 2.5 where $x = 0.2$. To inspect the effects from the polarization of PZT, an additional interface sheet charge was placed at the PZT/AlGaN interface (σ_{PZT}) to simulate the PZT polarization sheet charge, as shown in Fig. 4.2. Considering the fact that the polarization of the PZT layer is subjected to an external electric field, which will be provided by gate bias in this case, σ_{PZT} was restricted in the area under the gate electrode. In terms of the sign of σ_{PZT} , it should be positive if the direction of PZT polarization is parallel to that of the spontaneous polarization of AlGaN and negative if the former is antiparallel to the latter.

Table 4-1 Parameters used in Atlas simulation [26][27][28].

Parameter	GaN	AlGaN	PZT
Affinity (eV)	4.31	3.82	3.5
eg300 (eV)	3.4	3.96	3.3
align	0.8	0.8	—
permittivity	9.5	9.5	600
mun0 ($\text{cm}^2 \text{V}^{-1} \text{s}^{-1}$) ⁵	20	10	25
mup0 ($\text{cm}^2 \text{V}^{-1} \text{s}^{-1}$)	10	10	25
vsat (10^7 cm s^{-1})	1.9	1.1	—
nc300 (10^{18} cm^{-3})	1.07	2.07	140
nv300 (10^{19} cm^{-3})	1.16	1.16	34

⁵ In order to make the simulation results comparable to those of experiments, the electron mobility (mun0) of GaN and AlGaN were fitted against σ_{PZT} to 20 and 10 respectively, which is of course much too low compared to reported values ($900 \text{ cm}^2 \text{V}^{-1} \text{s}^{-1}$ for GaN and $600 \text{ cm}^2 \text{V}^{-1} \text{s}^{-1}$ for AlGaN). Possibly, the contact resistance of the devices was too high.

As for the important parameters used in Atlas simulation, the work function was set to 5.0 eV for gate (Ti/Au) and 4.2 eV for source and drain (Ti/Al) [25]. The value of σ_{PZT} was set to $0.4 \times 10^{13} \text{ cm}^{-2}$ to make the simulation results comparable to experiments, and this value applies to all simulations except for the simulations where σ_{PZT} was swept. The range of the sweep will be specified in the corresponding chapter. The other parameters used are listed in Table 4-1 [26][27][28]. Fermi-Dirac model was used for the carrier statistics. The impact ionization was assumed to occur only in GaN and Selberherr's model was adopted.

4.2 I-V characterization

The $I_d - V_{\text{ds}}$ characteristics of the simulated PZT-on-GaN HEMT is shown in Fig. 4.3 (a). The source voltage was set to 0 V and drain voltage was swept from 0 V to 15 V, where gate voltage was -2 V, -1 V, 0 V and 1 V respectively. The $I_d - V_{\text{gs}}$ characteristics is shown in Fig. 4.3 (b). The source voltage was set to 0 V and gate voltage was swept from -10 V to 1 V, where drain voltage was 0.25 V and 1 V, respectively.

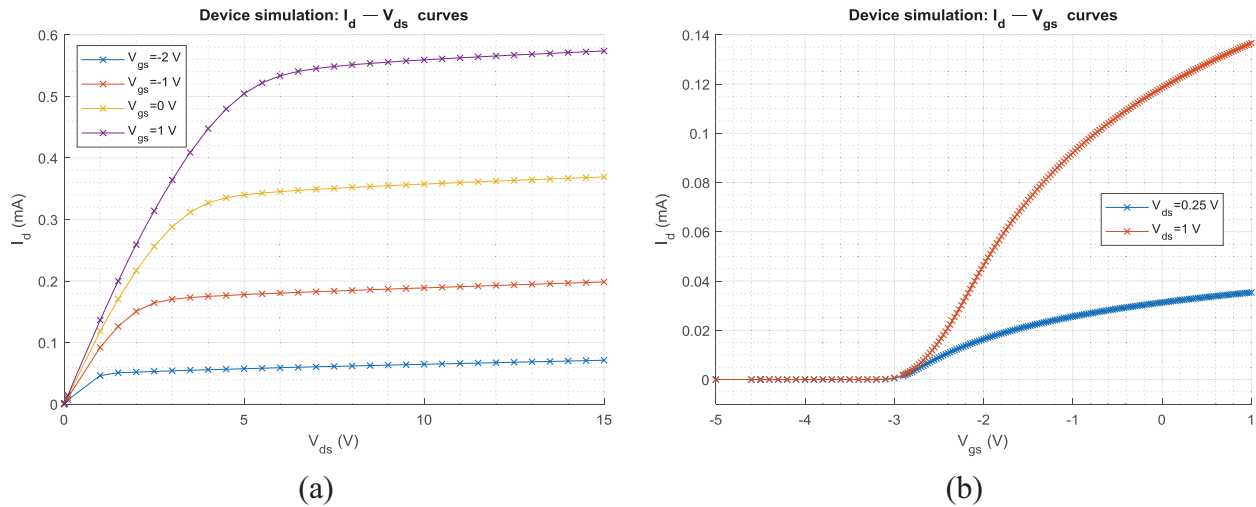


Fig. 4.3. The plot of $I_d - V_{\text{ds}}$ curves for different V_{gs} (a) and $I_d - V_{\text{gs}}$ curves for different V_{ds} (b) of the simulated PZT-on-GaN device.

From Fig. 4.3 (a) it can be seen that the simulated device exhibits typical output characteristics with good saturation properties. Fig. 4.3 (b) shows a typical transfer characteristics with a threshold voltage around -3 V, which is close to the typical value of -4 V exhibited by depletion-mode AlGaIn/GaN HEMTs [29].

4.3 Band diagram and 2DEG density

The purpose of this simulation is to study how the polarization of PZT influences the band offsets of the AlGaIn/GaN heterostructure and the 2DEG density. Without any bias on the electrodes, σ_{PZT} was swept from $-3 \times 10^{13} \text{ cm}^{-2}$ to $3 \times 10^{13} \text{ cm}^{-2}$. After running the script, the structure file was produced and then the information of band offsets and 2DEG density could be extracted from the outline of the structure file.

The comparison of band diagram at the AlGaIn/GaN heterostructure for three PZT polarization conditions is shown in Fig. 4.4. The three polarization conditions are “Antiparallel” for $\sigma_{\text{PZT}} = -3 \times 10^{13} \text{ cm}^{-2}$, “Zero” for $\sigma_{\text{PZT}} = 0$ and “Parallel” for $\sigma_{\text{PZT}} = 3 \times 10^{13} \text{ cm}^{-2}$, respectively. The distance between the conduction band and Fermi level determines the electron concentration, in particular at the AlGaIn/GaN interface the electrons accumulate. The deeper the penetration of the conduction band into Fermi level, the higher is the 2DEG density. Fig. 4.4 indicates that a PZT polarization which is parallel to the AlGaIn spontaneous polarization could increase the 2DEG density.

Furthermore, the dependency of n_{2d} on σ_{PZT} was extracted, as shown in Fig. 4.5. It can be seen that n_{2d} increases linearly when σ_{PZT} increases. Since n_{2d} governs the on-resistance and threshold voltage, this trend further suggests that R_{on} and V_{th} should decrease when σ_{PZT} increases parallel to spontaneous polarization of the AlGaIn layer.

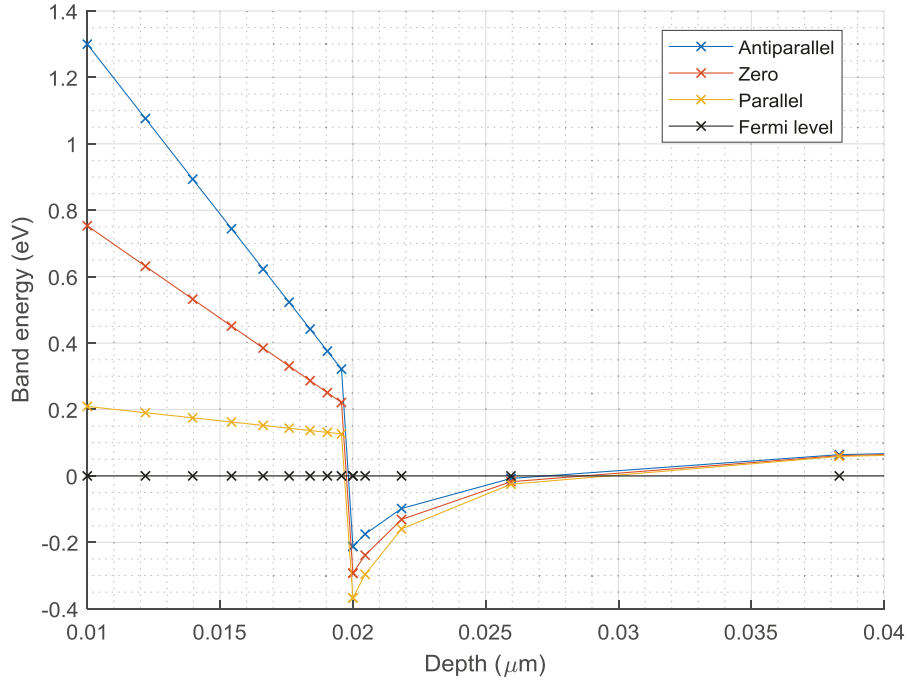


Fig. 4.4. Comparison of conduction band diagrams at the AlGaIn/GaN heterostructure for three PZT polarization conditions. The band energy was extracted from the cutline on each structure file. The coordinates of the cutline end points are (4,0) and (4,0.1), see Fig. 4.1. The legend “Antiparallel” stands for $\sigma_{\text{PZT}} = -3 \times 10^{13} \text{ cm}^{-2}$, “Zero” for $\sigma_{\text{PZT}} = 0$ and “Parallel” for $\sigma_{\text{PZT}} = 3 \times 10^{13} \text{ cm}^{-2}$. The black curve is the Fermi level.

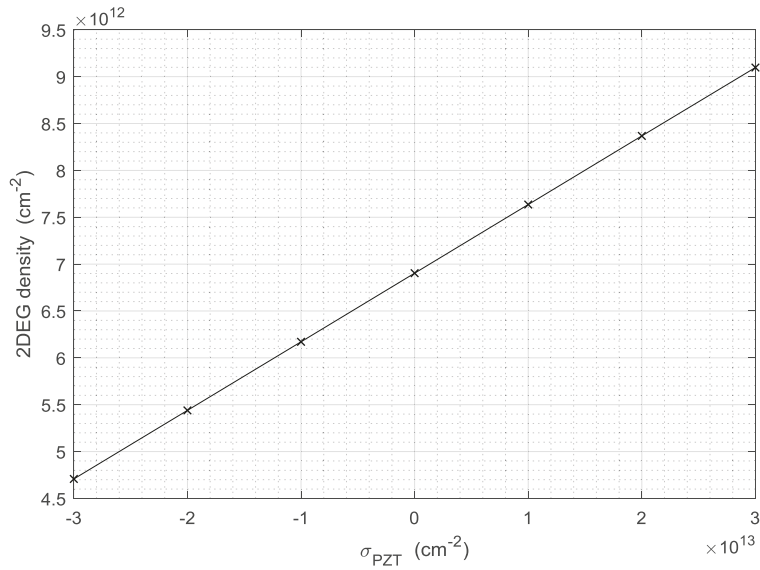


Fig. 4.5. The dependency of 2DEG density on σ_{PZT} .

4.4 On-resistance and threshold voltage

To investigate the dependence of R_{on} on L_{gd} , $I_{\text{d}} - V_{\text{ds}}$ curves were plotted for $L_{\text{gd}} = 2 \mu\text{m}$, $3 \mu\text{m}$, $5 \mu\text{m}$, $7 \mu\text{m}$ and $9 \mu\text{m}$ respectively, as shown in Fig. 4.6 (a). The slope of the fitting line in the linear region was taken as R_{on} . The relation between R_{on} and L_{gd} is shown in Fig. 4.6 (b) and it can be seen that R_{on} increases linearly with L_{gd} .

The influence of PZT polarization on R_{on} and V_{th} was inspected and their dependence on σ_{PZT} are demonstrated in Fig. 4.7 (a) and Fig. 4.7 (b) respectively. V_{th} was determined using the extrapolation in the linear region (ELR) method [30], *i.e.*, finding the V_{gs} axis intercept of the linear extrapolation of the $I_{\text{d}} - V_{\text{gs}}$ curve at its maximum slope point. Both R_{on} and V_{th} decrease when σ_{PZT} increases, which confirms the prediction in Chapter 4.3.

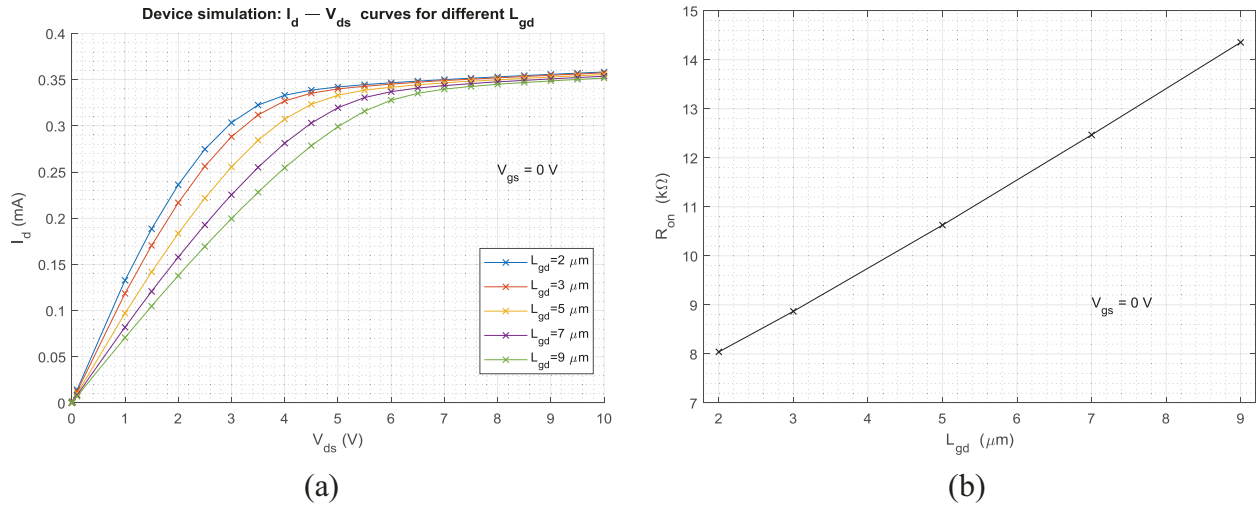


Fig. 4.6. The plot of $I_{\text{d}} - V_{\text{ds}}$ curves for different L_{gd} , where $V_{\text{gs}} = 0 \text{ V}$ (a). The dependence of R_{on} on L_{gd} (b). The reciprocal of the slope of the $I_{\text{ds}} - V_{\text{ds}}$ curve where $V_{\text{ds}} = 1 \text{ V}$ was adopted for determining the R_{on} .

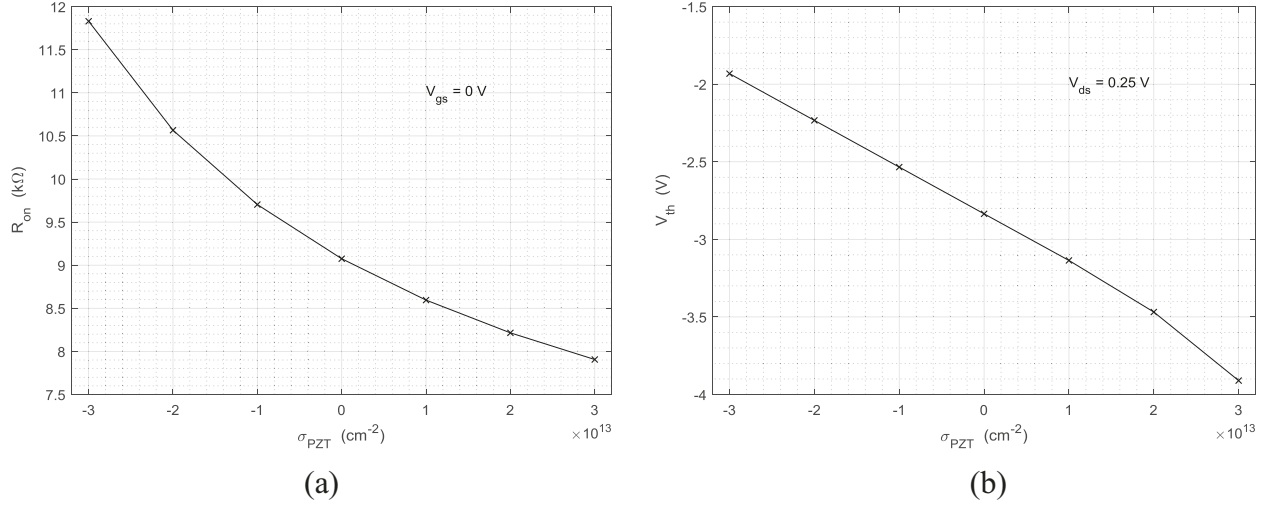


Fig. 4.7. The dependence of R_{on} on σ_{PZT} (a). The dependence of V_{th} on σ_{PZT} (b).

4.5 Subthreshold swing

The subthreshold swing (S) is defined as the gate voltage required to change the drain current by one order of magnitude, per decade, which can be expressed by

$$S = \frac{dV_{gs}}{d \log(I_d)}. \quad (4.1)$$

It reflects the easiness to switch from off-state to on-state. For the metal-oxide-semiconductor field-effect transistor (MOSFET), S can be calculated by [31]

$$S = \frac{kT}{q} (\ln 10) \left(1 + \frac{C_d}{C_{ox}} \right) \quad (4.2)$$

where k is Boltzmann's constant, q is the elementary charge, T is the temperature, C_d is the depletion layer capacitance, and C_{ox} is the gate-oxide capacitance. It has a theoretical limited of 60 mV/dec at room temperature. However for GaN HEMTs, experimental values of S have been reported to be 175 mV/dec [32] and 324 mV/dec [33]. In order to obtain the subthreshold swing of the simulated device, the $I_d - V_{gs}$ curves in Fig. 4.3 (b) were plotted in logarithmic scale, as shown in Fig. 4.8. The reciprocal of the slope of the linear fitting in the subthreshold region was

taken as S . It can be seen that S is about 112 mV/dec for $V_{ds} = 0.25$ V and 130 mV/dec for $V_{ds} = 1$ V.

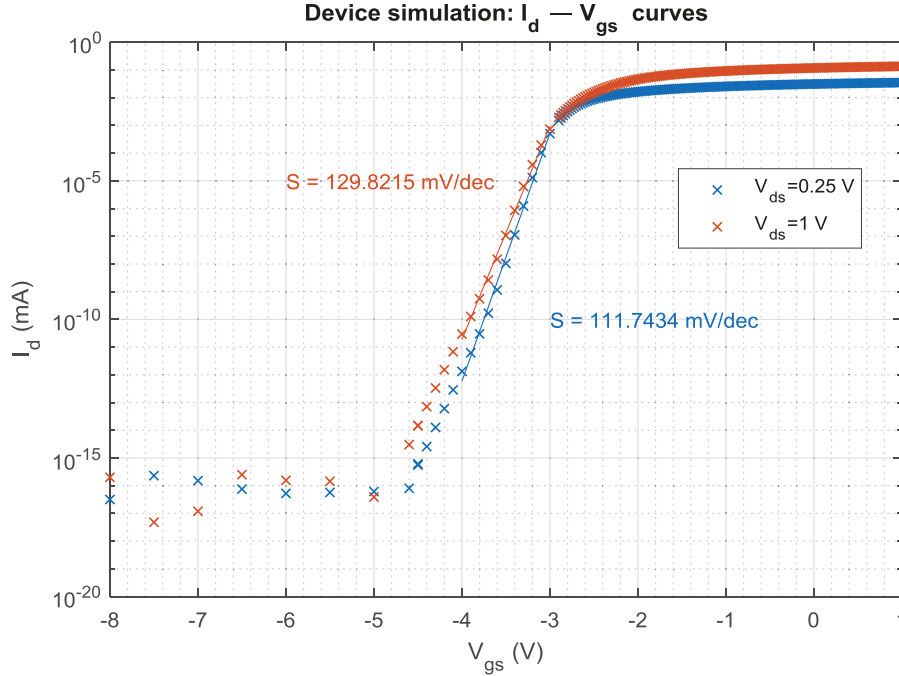


Fig. 4.8. The $I_d - V_{gs}$ plot on logarithmic scale for different different V_{ds} of the simulated PZT-on-GaN device. The linear fittings were performed in the subthreshold region. The value of S is about 112 mV/dec for $V_{ds} = 0.25$ V and 130 mV/dec for $V_{ds} = 1$ V.

4.6 Breakdown voltage

The breakdown voltage was investigated through simulation as well. To extract the breakdown voltage, the devices was simulated in off-state where the gate voltage was set to -5 V and source voltage set to 0 V. The drain voltage was swept from 0 V to 2000 V to obtain the $I_d - V_{ds}$ curve, and the intercept with x axis where the slope of the curve is maximum was adopted as BV . The off-state $I_d - V_{ds}$ curves for different L_{gd} were obtained, as shown in Fig. 4.9 (a) on linear scale

and Fig. 4.9 (b) on logarithmic scale. It can be seen from Fig. 4.9 (a) that BV increases as L_{gd} increases. The dependence of BV on L_{gd} is plotted in Fig. 4.10, which suggests that BV scales linearly with L_{gd} .

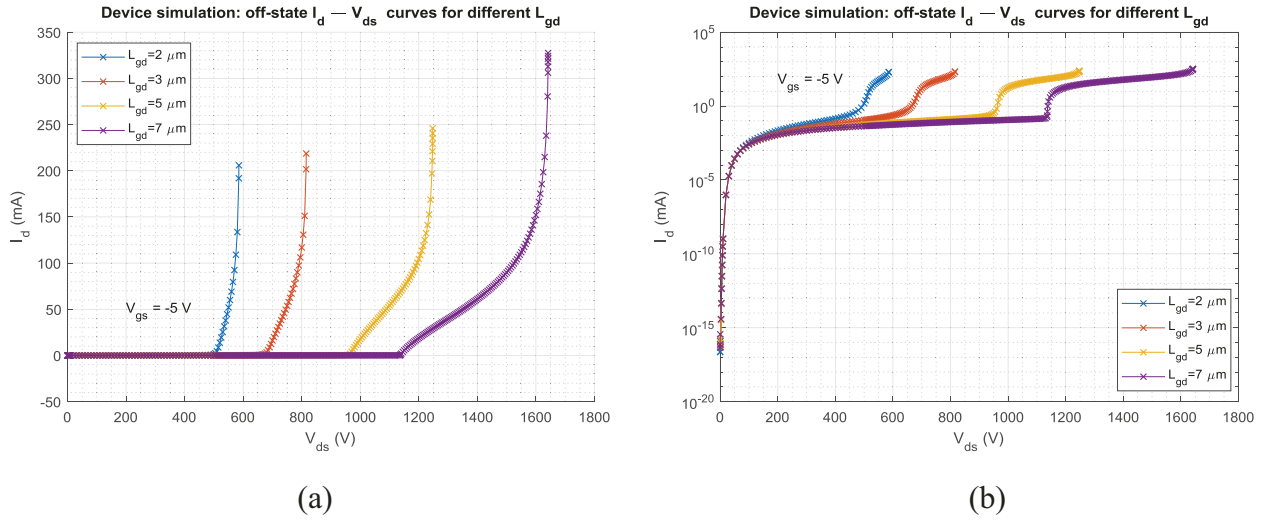


Fig. 4.9. The off-state $I_d - V_{ds}$ curves on linear scale (a) and logarithmic scale (b) with $L_{gd} = 2 \mu\text{m}$, $3 \mu\text{m}$, $5 \mu\text{m}$ and $7 \mu\text{m}$ respectively.

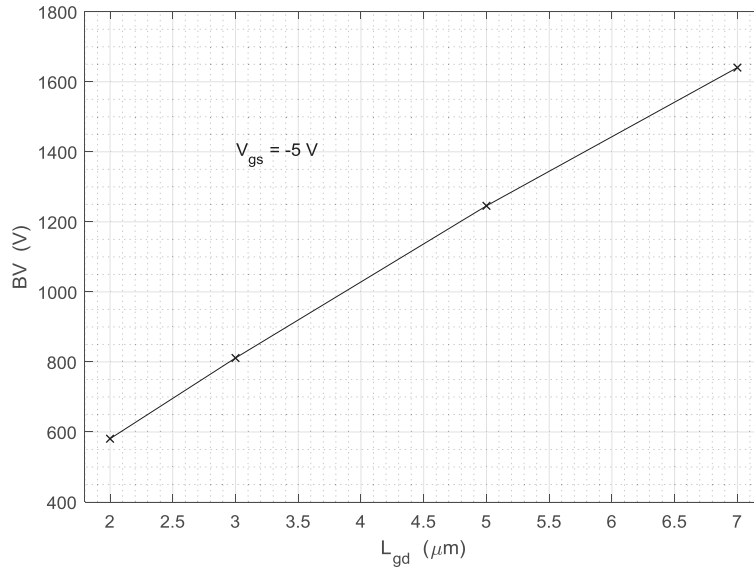


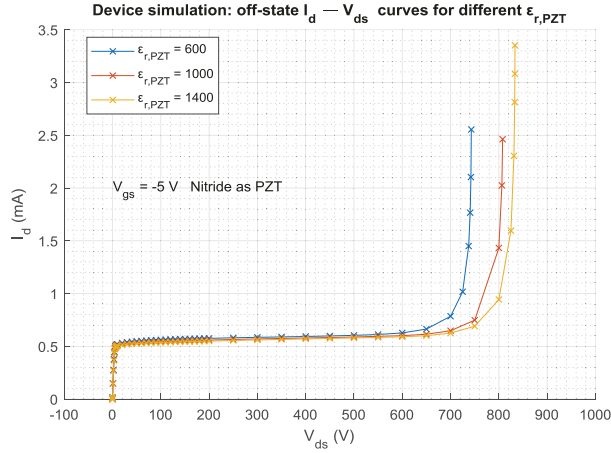
Fig. 4.10. The dependence of BV on L_{gd} .

It has been reported that a GaN-based HEMT in which the metal gate overlaps a high dielectric constant dielectric exhibits an increased BV [34], compared to one without the dielectric. Thus in this report it would be interesting to investigate how the permittivity of PZT ($\epsilon_{r,PZT}$) influences BV . However, during the simulations it was found that whether PZT is treated as semiconductor or insulator would lead to different results, which will be demonstrated separately in the following paragraph.

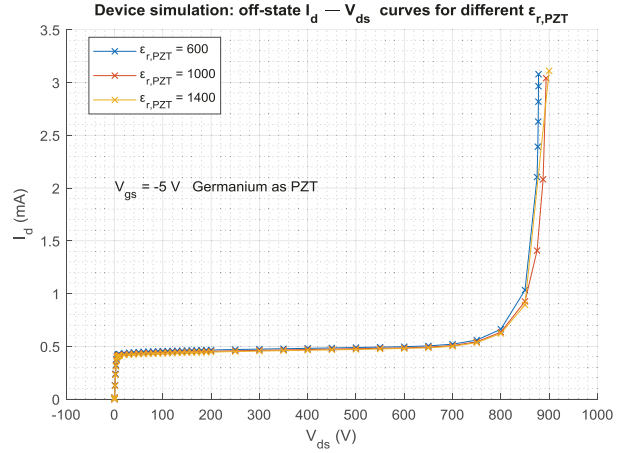
In the case where PZT was considered as an insulator, silicon nitride was used for the PZT layer. In addition, several geometric parameters of the model were modified, including a shift down of the gate ⁶ from PZT top surface to the PZT/AlGaN interface and the reduction of GaN thickness ⁷ from 1500 nm to 300 nm. In the other case where PZT was viewed as a semiconductor, germanium was used for the PZT layer and the geometric parameters were consistent with the former case. Similar to the acquisition of the off-state $I_d - V_{ds}$ curves for different L_{gd} , this time L_{gd} was fixed to 3 μm and $\epsilon_{r,PZT}$ was set to 600, 1000 and 1400 respectively. The results are shown in Fig. 4.11, with $I_d - V_{ds}$ curves for different $\epsilon_{r,PZT}$ where silicon nitride was adopted for the PZT layer on linear scale (a) and logarithmic scale (b), and germanium adopted for the PZT layer on linear scale (c) and logarithmic (d).

⁶ If not shifted down, the gate will be separated from the AlGaN/GaN layer by the insulating nitride.

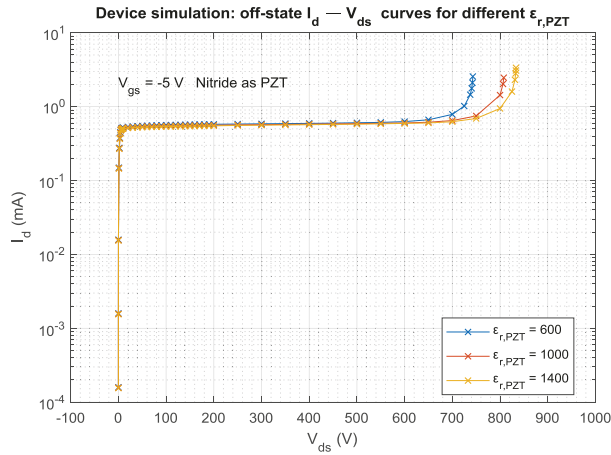
⁷ It was found that there would be current flowlines throughout the bulk GaN, if the thickness of GaN remained 1500 nm, which should not be the real case. After reducing the GaN thickness to 30 nm, the current would be limited to the narrow region near the AlGaN/GaN interface.



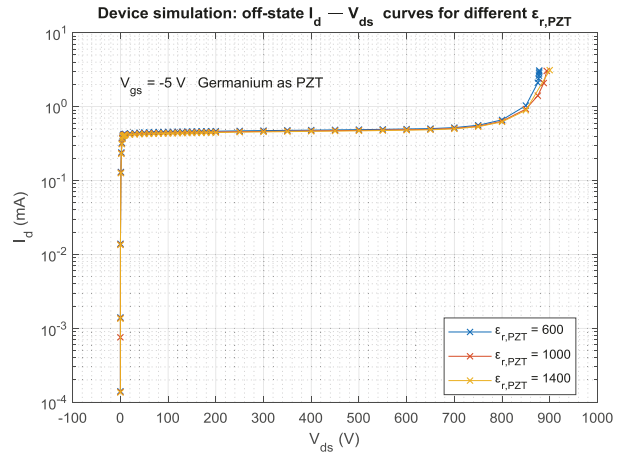
(a)



(c)



(b)



(d)

Fig. 4.11. Off-state $I_d - V_{ds}$ curves for different $\epsilon_{r,PZT}$ where silicon nitride was adopted for the PZT layer on linear scale (a) and logarithmic scale (b), and germanium adopted for the PZT layer on linear scale (c) and logarithmic scale (d).

It can be seen from Fig. 4.11 that BV increases as $\epsilon_{r,PZT}$ increases when PZT is regarded as insulator, while BV does not scale with $\epsilon_{r,PZT}$ when PZT is regarded as semiconductor. In order to further investigate the reason, the distribution of the lateral electric field (E_x) along the conduction channel was examined, which was extracted through a horizontal cutline near the GaN top surface at the moment of breakdown, as shown in Fig. 4.12. The peak value of E_x in both Fig.

4.12 (a) and (b) is around $-320 \text{ V}/\mu\text{m}$, which is in accordance with the theoretical critical field of GaN. However the distributions of E_x in two cases differ from each other.

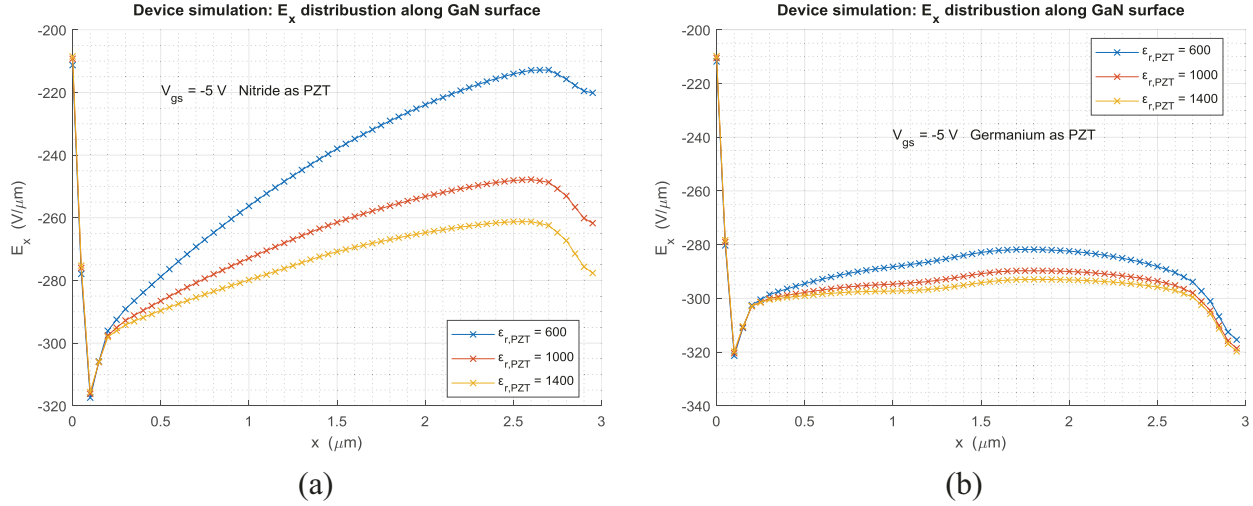


Fig. 4.12. The distribution of lateral electrical field (E_x) along the conduction channel, where silicon nitride was adopted for the PZT layer (a) and germanium adopted for the PZT layer (b). The position $x = 0$ corresponds to the gate edge and $x = 3$ corresponds to the drain edge. The coordinates of the cutline end points are (5,0.021) and (8,0.021) in Fig. 4.1.

In Fig. 4.12 (a) the uniformity of E_x distribution is increased by a larger $\epsilon_{r,PZT}$, thus results in a higher BV . In other words, given the same drain voltage before breakdown, a larger $\epsilon_{r,PZT}$ leads to a flatter distribution of E_x and smaller peak value of E_x , and consequently the device with the smallest $\epsilon_{r,PZT}$ will first breakdown and the devices with higher $\epsilon_{r,PZT}$ can withstand higher drain voltages until the critical field is reached. The similar effect has been reported as the dielectric modulated reduced surface field (RESURF) [35].

As a comparison, in Fig. 4.12 (b) the E_x distribution is almost the same for all three $\epsilon_{r,PZT}$ conditions, which is in accordance with the result in Fig. 4.11 (b) that the values of BV are close to each other. This finding implies that the distribution of E_x is not or little subjected to the permittivity of the layer deposited on AlGaN if it is conducting. Instead, it is flattened because of the

current flow of the layer. This principle is applied in the semi-insulating RESURF to increase BV [36] [37].

5 Electrical Characterization

The electrical measurement results are presented in this chapter. It starts with the subsection of functionality check of all devices on the chips, followed by the output characteristics, transfer characteristics, and ended with off-state breakdown. In each subsection, the characterization results are analyzed and compared amongst the devices. Due to the large amount of devices and related data, it is not practical to address all of them in this report. Therefore, certain “typical” devices will be selected as an example. For convenience sake, the devices in the same row on a chip will be referred to as “series”. For instance, series “2-X-1” refers to the devices with varying L_{gd} while L_{sg} fixed to $2\ \mu\text{m}$ and the overlap fixed to $1\ \mu\text{m}$. The comparisons will be conducted amongst the devices within the same series, as well as the ones with the same label but on different chips (*i.e.*, different Zr compositions). To present a clearer view, some $I - V$ curves are plotted in a single sweep, although they were measured in a dual sweep. Unless stated otherwise, these $I - V$ curves are based on data in the second half of the dual sweep.

5.1 Devices functionality check

During the initial preliminary on-state measurements it was found that not all devices were functioning properly. In the $I_d - V_{gs}$ measurement, some devices did not show the gating effect, *i.e.*, the drain current remained almost constant and did not change with gate voltage. For the $I_d - V_{ds}$ measurements, several devices exhibited a rapidly growing drain current which reached the compliance when V_d was only 0.25 V. These deviant devices were not functional and not suitable for the analysis. Therefore it was necessary to check the condition of all devices, and only the ones of which both $I_d - V_{ds}$ and $I_d - V_{gs}$ characteristics were normal would be viewed as properly functioning. The test results are summarized in Table 5-1. The labels in shadow represent the deviant devices that are not properly functioning. It should be mentioned that Table

5-1 is only valid for on-state characterization before the breakdown measurements, because some of the devices were destroyed during breakdown.

Table 5-1 Functionality check of the devices (only valid before breakdown measurement). Refer to Fig. 3.1 (b) for the chip layout.

08282016-1 (100 nm 20/80)				
2-9-1	2-7-1	2-5-1	2-3-1	2-2-1
2-9-0.5	2-7-0.5	2-5-0.5	2-3-0.5	2-2-0.5
1.5-8-0.5	1.5-6-0.5	1.5-4-0.5	1.5-3-0.5	1.5-2-0.5
3-8-0.5	3-6-0.5	3-4-0.5	3-3-0.5	3-2-0.5
3-8-1	3-6-1	3-4-1	3-3-1	3-2-1
08262016-3 (50 nm 52/48)				
2-9-1	2-7-1	2-5-1	2-3-1	2-2-1
2-9-0.5	2-7-0.5	2-5-0.5	2-3-0.5	2-2-0.5
1.5-8-0.5	1.5-6-0.5	1.5-4-0.5	1.5-3-0.5	1.5-2-0.5
3-8-0.5	3-6-0.5	3-4-0.5	3-3-0.5	3-2-0.5
3-8-1	3-6-1	3-4-1	3-3-1	3-2-1
08282016-4 (100 nm 80/20)				
2-9-1	2-7-1	2-5-1	2-3-1	2-2-1
2-9-0.5	2-7-0.5	2-5-0.5	2-3-0.5	2-2-0.5
1.5-8-0.5	1.5-6-0.5	1.5-4-0.5	1.5-3-0.5	1.5-2-0.5
3-8-0.5	3-6-0.5	3-4-0.5	3-3-0.5	3-2-0.5
3-8-1	3-6-1	3-4-1	3-3-1	3-2-1

5.2 Output characteristics

Devices in series “2-X-1” on chip “20/80” and “52/48” are taken as an example to illustrate the output characteristics of the PZT-on-GaN HEMTs. The results for chip “20/80” are shown in Fig. 5.1. The comparison of $I_d - V_{ds}$ curves of series “2-X-1” is shown in Fig. 5.1 (a), with a dual sweep of V_d from 0 V to 6 V and then back to 0 V. For device “2-3-1”, the $I_d - V_{ds}$ and $I_g - V_{ds}$ curves at different V_{gs} are shown in (b) and (d), respectively, together with the extraction of R_{on} in (c). Similarly, the results for chip “52/48” are shown in Fig. 5.2.

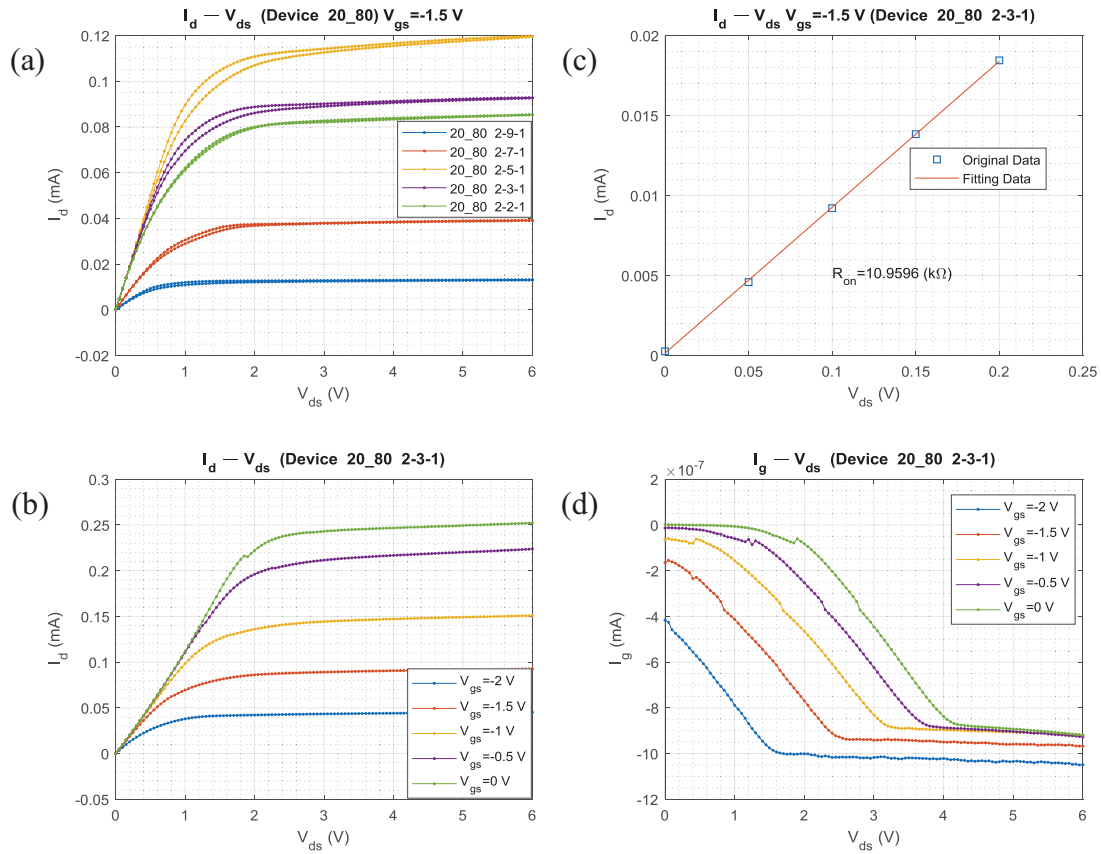


Fig. 5.1. The overview of the output characteristics of the measured devices on chip “20/80”. The comparison of $I_d - V_{ds}$ curves of series “2-X-1” is shown in (a) with a dual sweep of V_d , where $V_{gs} = -1.5$ V. The $I_d - V_{ds}$ curves of device “2-3-1” at different V_{gs} are shown in (b), together with the extraction of R_{on} in (c) and $I_g - V_{ds}$ curves in (d).

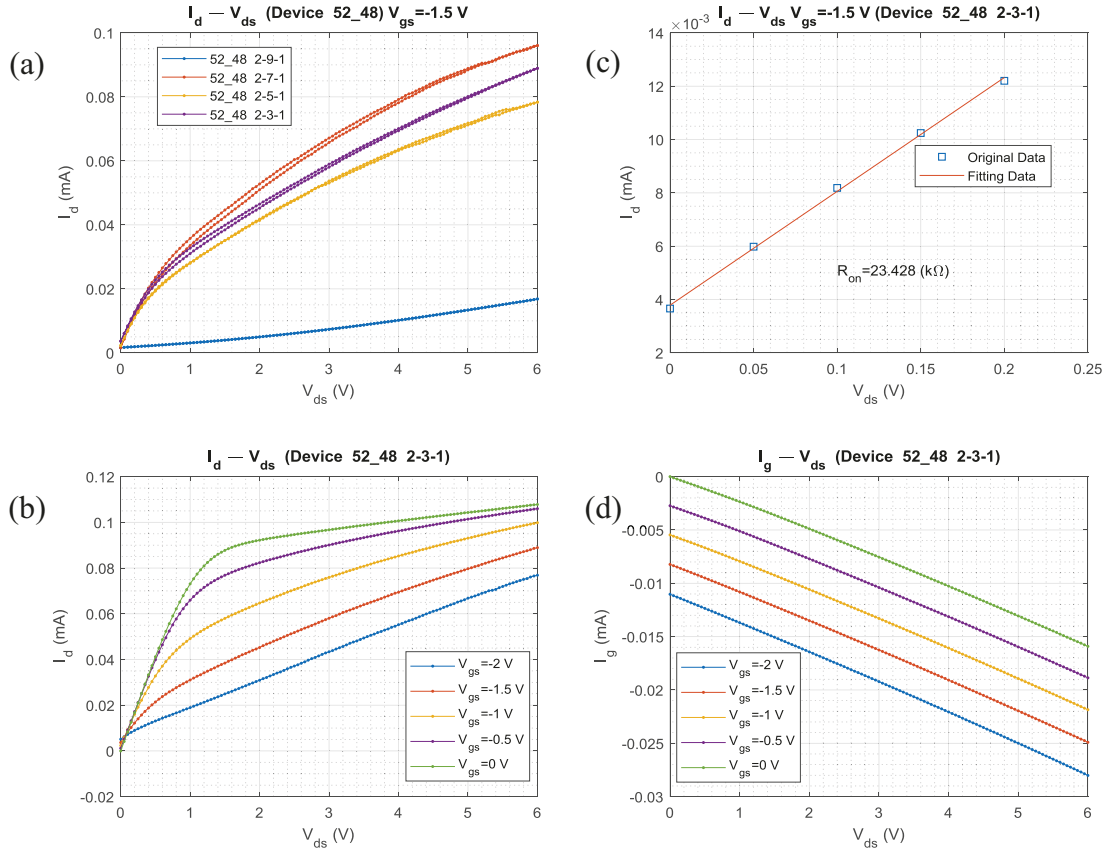


Fig. 5.2. The overview of the output characteristics of the measured devices on chip "52/48". The comparison of $I_d - V_{ds}$ curves of series "2-X-1" is shown in (a) with a dual sweep of V_{ds} , where $V_{gs} = -1.5$ V. The $I_d - V_{ds}$ curves of device "2-3-1" at different V_{gs} are shown in (b), together with the extraction of R_{on} in (c) and $I_g - V_{ds}$ curves in (d).

It can be seen in Fig. 5.1 (a) that the five devices in series "2-X-1" on chip "20/80" exhibit typical $I_d - V_{ds}$ characteristics with both a linear region and saturation region. Moreover, a deviation can be found between the two curves within a dual sweep, and such difference is more obvious for devices with a shorter L_{gd} . This could be related to the flip of the horizontal polarization of PZT, which is caused by the direction change of the lateral electric field at the turning point of the dual sweep. Since V_{ds} is the same for all devices in series "2-X-1", the lateral electric

field can be higher for devices with shorter L_{gd} , and thus results in stronger influence on the horizontal polarization. For device “20/80 2-3-1”, the saturation current is around 0.09 mA, which is comparable to the simulation result in Fig. 4.3 (a). In Fig. 5.1 (b) the saturation current is increasing with V_{gs} , however the intervals between the adjacent curves are not identical. Fig. 5.1 (d) shows a low gate leakage, which suggests that PZT can be conducting. According to Fig. 5.1 (c), R_{on} is calculated as 11.0 k Ω at $V_{gs} = -1.5$ V. Since the gate width is 30 μm and the device pitch for “2-3-1” is roughly 7 μm , $R_{on,sp}$ is calculated to be 23.1 m $\Omega \cdot \text{cm}^2$.

However, the $I_d - V_{ds}$ curves for devices on chip “52/48” in Fig. 5.2 (a) do not show a saturation behavior. Instead, I_d continues to increase when V_{ds} is beyond the saturation point. This observed trend is very likely to be linked to the channel length modulation (CLM) effects. The CLM effect for AlGaIn/GaN HEMTs has been reported and modeled in related researches [38]. Compared to Fig. 5.1 (d), Fig. 5.2 (d) shows a much higher gate leakage, which increases linearly with V_{ds} . The same behavior is also observed for the other series on chip “52/48”. Comparing Fig. 5.2 (b) to (d), it can be seen that for device “2-3-1” at $V_{ds} = 6$ V, I_d is around 0.11 mA while I_g already reaches -0.016 mA, which accounts for almost 15% of I_d . This finding implies a substantial conduction current flow through PZT for devices on chip “52/48”, which obviously is not desired. According to Fig. 5.2 (c), R_{on} for device “52/48 2-3-1” is calculated as 23.4 k Ω at $V_{gs} = -1.5$ V, which is almost twice the value of device “20/80 2-3-1”.

The on-resistance of the other devices in series “2-X-1” on chip “20/80” are calculated the same way as device “20/80 2-3-1” shown in Fig. 5.1 (c). The function of R_{on} on L_{gd} is plotted in Fig. 5.3. It can be seen that R_{on} scales with L_{gd} when L_{gd} is larger than 5 μm . Nevertheless, it remains to be the same when L_{gd} is below 5 μm , which is contradictory to both theoretical analysis and the simulation result presented in Fig. 4.6 (b). Possible explanations could be that there

was a misalignment of the masks during the lithography process and the real geometric size may not be what was expected. It could also be that a large lateral electric field induced by a short L_{gd} alters the horizontal polarization of PZT and thus influences the 2DEG density. In addition, a variable contact resistance could severely affect this trend. Consequently, R_{on} stops scaling down with L_{gd} .

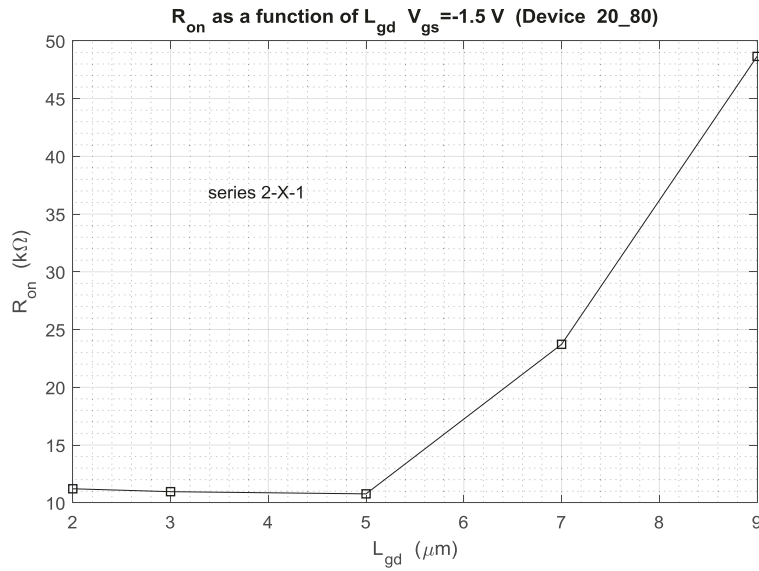


Fig. 5.3. The function of R_{on} on L_{gd} for series “2-X-1” on chip “20/80”, with $V_{gs} = -1.5$ V.

Devices on chip “80/20” have similar output characteristic to those on chip “20/80”. The extent of CLM effect is between the devices on chip “20/80” and “52/48”. For device “80/20 2-3-0.5”, the gate leakage has a magnitude of 10^{-5} mA and R_{on} is around 20.7 k Ω when $V_{gs} = -1.5$ V.

5.3 Transfer characteristics

In consistence with the previous characterization, the same devices are taken as an example to illustrate the transfer characteristics of the PZT-on-GaN HEMTs. The comparison of $I_d - V_{gs}$ curves of the devices in series “2-X-1” are shown in Fig. 5.4 (a) for chip “20/80” and Fig. 5.4 (b) for chip “52/48” respectively, where $V_{ds} = 0.25$ V. To investigate more parameters, device “20/80 2-3-1” and “52/48 2-3-1” are selected for illustration purpose. For device “20/80 2-3-1”, the characterization results are summarized in Fig. 5.5, with the $I_d - V_{gs}$ curves at different V_{ds} on linear scale in (a) and logarithmic scale in (b), the $I_g - V_{gs}$ curves at different V_{ds} in linear scale in (d) and logarithm scale in (e), the plot of g_m as a function of V_{gs} in (c), and the plot of $\log_{10}(I_d) - V_{gs}$ for calculation of S in (f). The data for device “52/48 2-3-1” are shown the same way in Fig. 5.6.

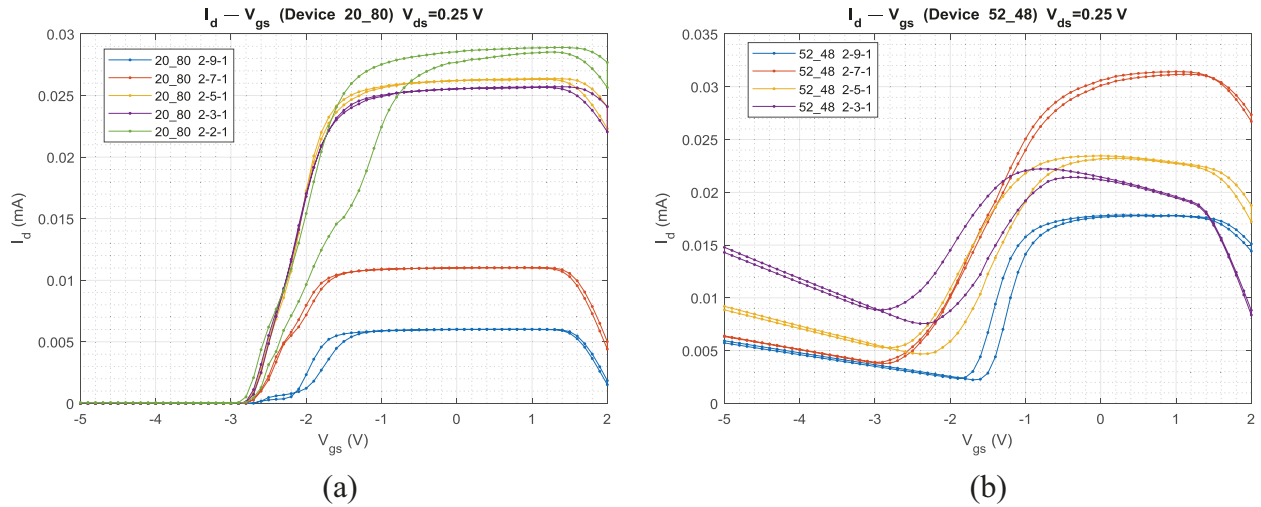


Fig. 5.4. The comparison of $I_d - V_{gs}$ curves of the devices in series “2-X-1” for chip “20/80” (a) and “52/48” (b) with a dual sweep of V_g , where $V_{ds} = 0.25$ V.

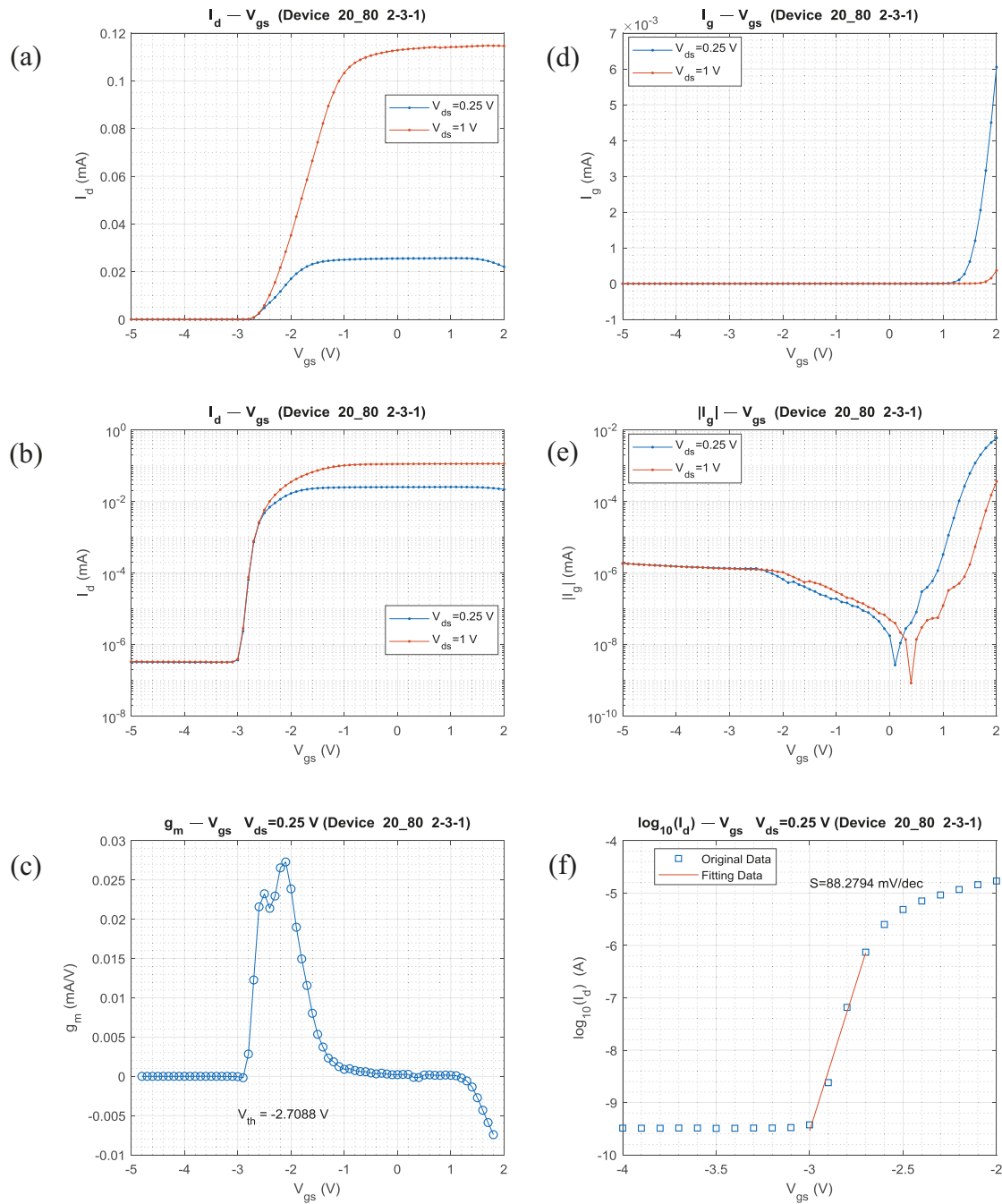


Fig. 5.5. The overview of the transfer characteristics of device “20/80 2-3-1”. $I_d - V_{gs}$ curves for different V_{ds} on linear scale (a) and logarithmic scale (b). $I_g - V_{gs}$ curves for different V_{ds} on linear scale (d) and logarithmic scale (e). g_m as a function of V_{gs} (c). $\log_{10}(I_d) - V_{gs}$ curve for calculating S (f).

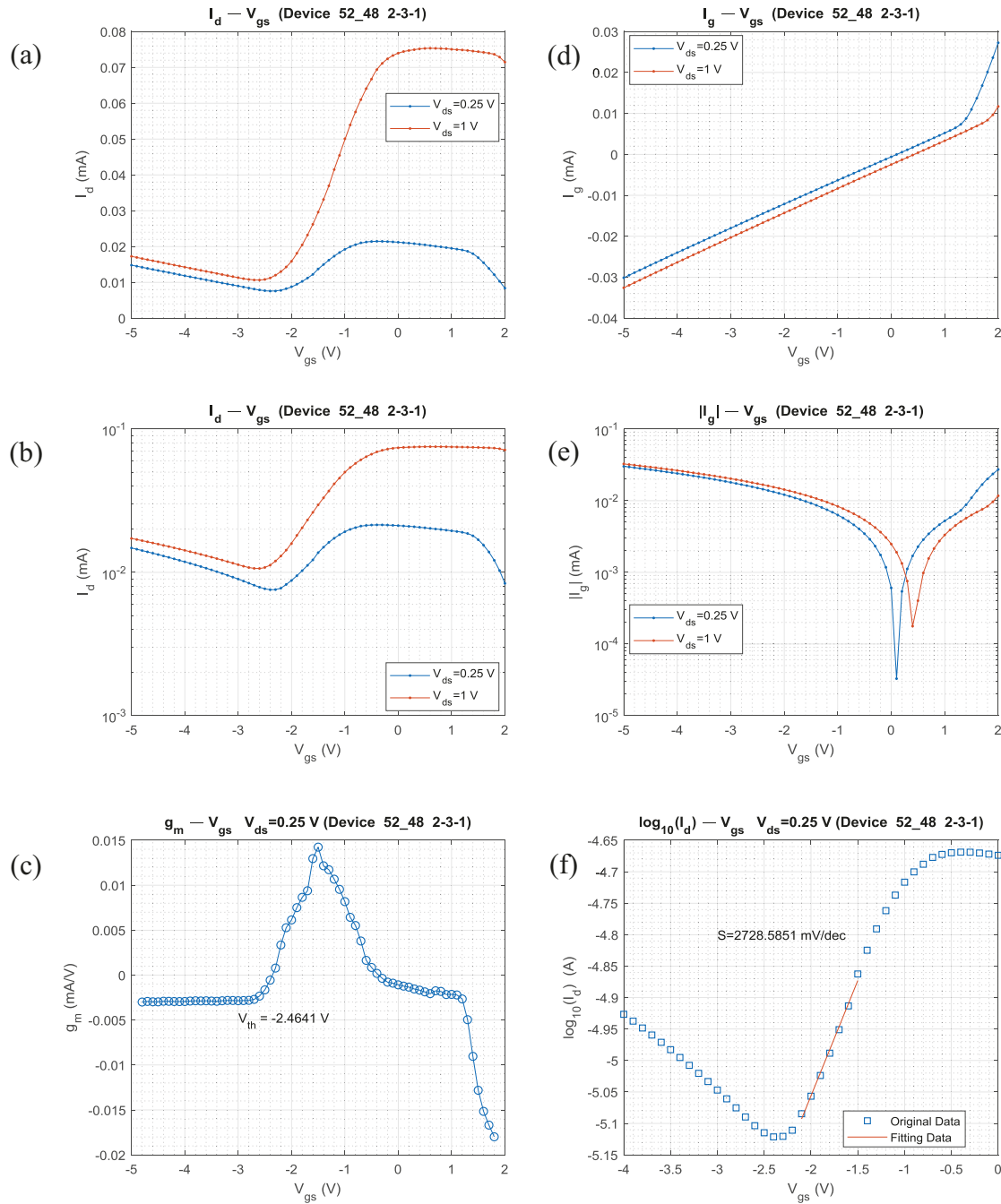


Fig. 5.6. The overview of the transfer characteristics of device “52/48 2-3-1”. $I_d - V_{gs}$ curves for different V_{ds} on linear scale (a) and logarithmic scale (b). $I_g - V_{gs}$ curves for different V_{ds} on linear scale (d) and logarithmic scale (e). g_m as a function of V_{gs} (c). $\log_{10}(I_d) - V_{gs}$ curve for calculating S (f).

Fig. 5.4 shows that the devices exhibit a typical $I_d - V_{gs}$ characteristic when V_{gs} is lower than 1 V. Some devices shown an obvious deviation of the two curves within a dual sweep and the shape resembles a hysteresis loop, but other devices show little deviations. Therefore, it is difficult to confirm whether it is caused by the changing polarization of PZT or random measurement errors/process variation. For device “20/80 2-3-1” in Fig. 5.5 where $V_{ds} = 0.25$ V, V_{th} is about -2.7 V and the saturation current is about 0.026 mA. For device “52/48 2-3-1” in Fig. 5.6, V_{th} is about -2.5 V and the saturation current is about 0.022 mA. The measured threshold voltages are close to the simulation results of -3 V in Chapter 4.2. It should be mentioned that the ELR method is still adopted here to determine V_{th} . However, as can be seen in Fig. 5.5 (c), g_m is a multi-extreme value function of V_{gs} , and some other devices show the same behavior. In such situation, the first appeared extreme value is taken.

Further, Fig. 5.4 shows that I_d begins to drop when V_{gs} is beyond 1.4 V. The cause can be found in Fig. 5.5 (d) and Fig. 5.6 (d), where I_g suddenly rises when V_{gs} is around 1.4 V. Furthermore, by checking Fig. 5.5 (d) and (e) together, it can be confirmed that the $I_g - V_{gs}$ curve has a typical rectifier diode feature. This behavior has been reported as “diode forward turn on” [39] in a conventional AlGaIn/GaN HEMT without PZT, where the gate (anode), AlGaIn/GaN layer and drain (cathode) form a Schottky barrier diode (SBD). When V_{gs} is beyond the diode forward turn-on voltage (V_F) which is typically between +1 V to +2 V, the SBD will be in forward operation. For the case of the PZT-on-GaN HEMTs the PZT layer acts as a semiconductor and therefore in this material an SBD can be formed [40] [41]. For the PZT-on-GaN HEMTs in this report, V_F is around 1.4 V. The occurrence of the “diode forward turn on” behavior in PZT-on-GaN HEMTs indeed confirms that PZT is conducting, because the carriers have to cross through the PZT layer.

Another peculiar phenomenon is the leakage current of the “52/48” devices observed in Fig. 5.6 (a) and (b), where I_d is still substantial despite the fact that V_{gs} is below -3 V. In addition, I_d decreases with increasing V_{gs} when it is below -3 V. Correspondingly in Fig. 5.6 (d) and (e) I_g is relatively high. Since Fig. 5.5 (d) and (e) have revealed an SBD between the gate and drain, it should be switched off under reverse bias. Based on this point, the non-zero part of I_g in Fig. 5.6 (d) and (e) could originate via another conduction path.

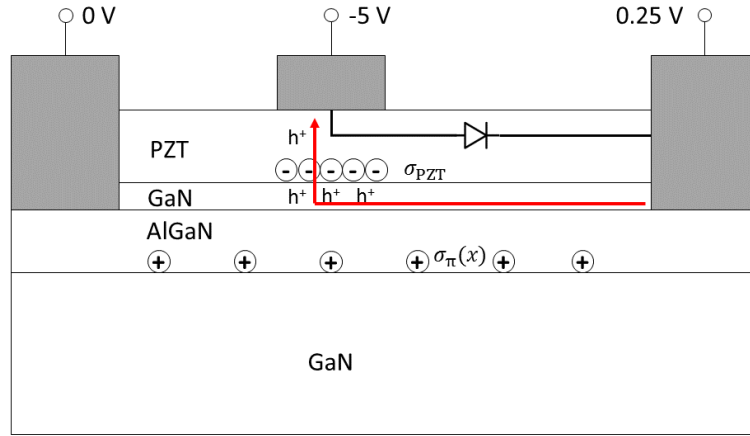


Fig. 5.7. The description of the hole induced gate leakage hypothesis. A Schottky barrier diode has formed between gate and drain. In a real device, there is a very thin GaN layer between the PZT layer and the AlGaN layer. When $V_{gs} = -5V$, σ_{PZT} is estimated to be $-5 \times 10^{14} \text{ cm}^{-2}$. Therefore, holes could accumulate in the thin GaN layer and form a conduction channel with PZT.

Therefore, a hypothetical “hole induced gate leakage model” has been proposed in this report to explain the behavior of devices on chip “52/48” described above. The model is shown in Fig. 5.7. The SBD which will be switched off when $V_{gs} < 1.4 \text{ V}$. Considering the vertical coercive field is roughly 40 kV/cm ($4 \text{ V}/\mu\text{m}$, see Chapter 2.3) and the thickness of PZT is 50 nm, then the voltage drop over the PZT layer required to convert the direction of PZT polarization is 0.2 V. Therefore when $V_{gs} = -5 \text{ V}$ the vertical polarization of PZT should be pointing towards the gate,

thus σ_{PZT} will be negative. The value of σ_{PZT} for devices on chip “52/48” can be estimated from the saturation polarization (P_s) of PZT with the 0.52 Zr composition, which is roughly $80 \mu\text{C}/\text{cm}^2$, see Fig. 2.7 (a). Therefore σ_{PZT} is estimated to be $-5 \times 10^{14} \text{ cm}^{-2}$. Because of the negative and large σ_{PZT} , holes can accumulate in the thin GaN layer and then form a conduction channel with PZT, which could be the origin of the gate leakage. This explanation is self-consistent with the fact observed in Fig. 5.6 (a) that I_d decreases with increasing V_{gs} when $V_{\text{gs}} < -3 \text{ V}$, since an increasing gate voltage will reduce the number of holes at the conduction channel. As a comparison, the saturation polarization of PZT with 0.2 Zr composition is reported to be half the value of PZT with 0.52 composition. Therefore, in this case σ_{PZT} may not be strong enough to make the holes accumulate and I_d is close to zero.

In terms of subthreshold swing, S is around $88 \text{ mV}/\text{dec}$ for device “20/80 2-3-1”, which is comparable to the theoretical limit of $60 \text{ mV}/\text{dec}$ and the simulation result of $112 \text{ mV}/\text{dec}$. This result suggests that device “20/80 2-3-1” has a satisfactory switching characteristic. For device “52/48 2-3-1”, theoretically S cannot be calculated because V_{th} is out of the linear region. However, if ignoring the limitation by V_{th} , S incredibly large around $2729 \text{ mV}/\text{dec}$, which could be caused by the dramatically high gate leakage current, obviously not desired.

5.4 Off-state breakdown

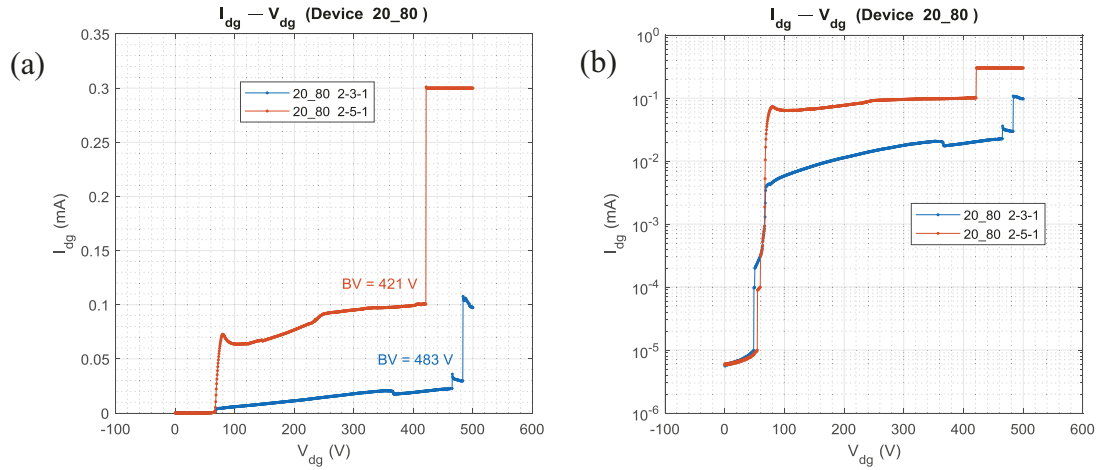


Fig. 5.8. Breakdown voltage measurement of device “2-3-1” and “2-5-1” on chip “20/80”. The measured $I_{dg} - V_{dg}$ curves on linear scale (a) and logarithmic scale (b).

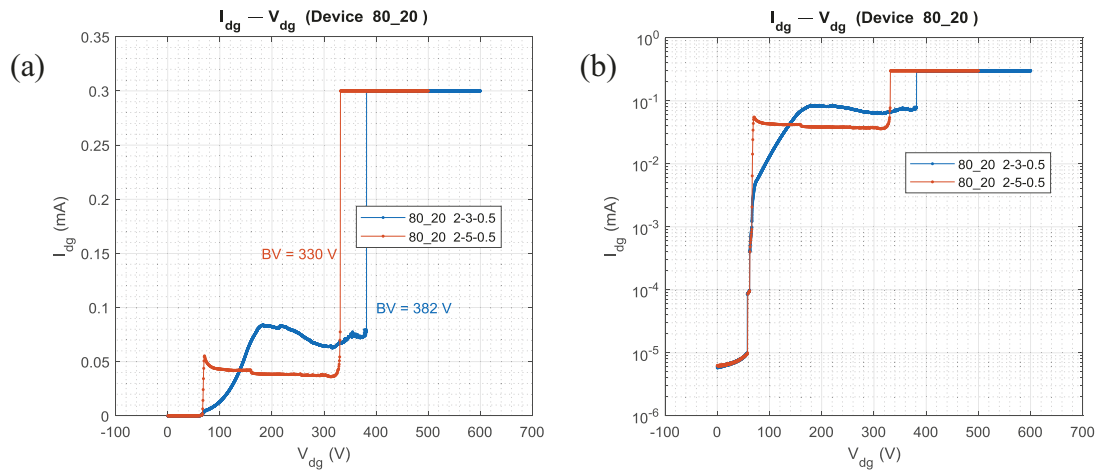


Fig. 5.9. Breakdown voltage measurement of device “2-3-1” and “2-5-1” on chip “80/20”. The measured $I_{dg} - V_{dg}$ curves on linear scale (a) and logarithmic scale (b).

It was found that breakdown measurement was destructive and the devices were destroyed after breakdown. In order not to destroy all devices, only four devices were measured. Due to the complexity of wire bonding and the Keithley instrument used for the measurement, the gate-

drain breakdown was measured instead of a three-terminal breakdown. The breakdown voltage measurement result is shown in Fig. 5.8 for devices on chip “20/80” and Fig. 5.9 for devices on chip “80/20”, with $I_{dg} - V_{dg}$ curves on linear scale in (a) and logarithmic scale in (b). A current criterion of 0.1 mA is used for defining BV , *i.e.*, the V_{dg} where I_{dg} reaches 0.1 mA is adopted as BV . The results are $BV = 483$ V, 421 V, 382 V and 330 V for device “20/80 2-3-1”, “20/80 2-5-1”, “80/20 2-3-0.5” and “80/20 2-5-0.5” respectively.

However, a two-step breakdown can be observed from Fig. 5.8 and Fig. 5.9, as well as a poor scaling of BV with L_{gd} , which could be caused by degradation of the device or poor edge termination (see Fig. 3.1 (b)). The possible poor edge termination could be attributed to the rectangular mask layout designs. Therefore, more dedicated test structures are needed to have a better result and analysis. To confirm whether the PZT layers can increase BV , a reference device without PZT is needed.

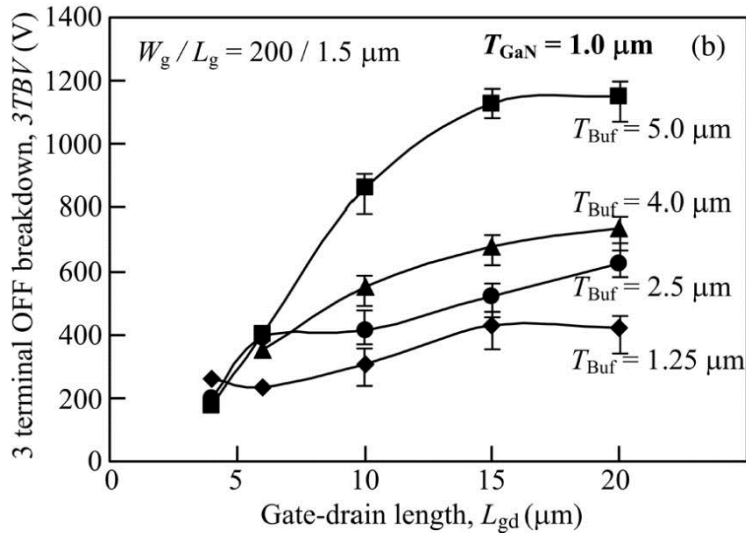


Fig. 5.10. Summary of BV of HEMTs with various L_{gd} from literature [43].

According to related literature, BV has been observed to be 1370 V with $L_{gd} = 18 \mu\text{m}$ and $W = 100 \mu\text{m}$ [42] and 1402 V with $L_{gd} = 20 \mu\text{m}$ and $W = 200 \mu\text{m}$ [43]. More results of BV for various L_{gd} from literature are summarized in Fig. 5.10. The comparison of the BV observed in this report and from literature is shown in Table 5-2.

Table 5-2 Comparison of breakdown voltages observed in this report and those from literature.

	From experiments of this report				From literature		
	20/80		80/20		5	18	20
L_{gd}	3	5	3	5	5	18	20
BV (V)	483	421	382	330	300	1370	1402
BV/L_{gd} (V/ μm)	161.0	84.2	127	66	60.0	76.1	70.1

As can be seen from Table 5-2, the ratio of BV/L_{gd} is much lower than the ideal GaN theoretical critical field ($E_c = 330 \text{ V}/\mu\text{m}$). Possible explanations could be the imperfections arising out of the growth of GaN [44]. In addition, E_c for the lateral breakdown may not be as high as $330 \text{ V}/\mu\text{m}$ due to the anisotropic property of GaN. Nevertheless, in terms of BV/L_{gd} ratio, the results of device “20/80 2-5-1” and “80/20 2-5-1” are close to the reported values from literature, and the ratios of the other two devices are higher.

5.5 Summary

A comparison of R_{on} for various devices are summarized in Table 5-3, where the label “Difference” is defined as $\Delta R_{\text{on}} = R_{\text{on},V_{\text{gs}}=-1.5\text{V}} - R_{\text{on},V_{\text{gs}}=0\text{V}}$. For all devices, it can be found that $\Delta R_{\text{on}} > 0$, in other words, R_{on} reduces with V_{gs} , which is in agreement with theory. Furthermore, a clear trend is that $\Delta R_{\text{on}}(52/48) \gg \Delta R_{\text{on}}(80/20) > \Delta R_{\text{on}}(20/80)$ and that $R_{\text{on}}(52/48)$ is almost halved when V_{gs} increases from -1.5 V to 0 V. This reduction is very likely to be related to the PZT polarization, besides the increasing V_{gs} .

Table 5-3 Comparison of R_{on} for various devices

R_{on} (k Ω)	2-3-1			2-5-1		
	$V_{\text{gs}} = -1.5\text{ V}$	$V_{\text{gs}} = 0\text{ V}$	Difference	$V_{\text{gs}} = -1.5\text{ V}$	$V_{\text{gs}} = 0\text{ V}$	Difference
20/80	11.0	9.9	1.1	10.8	9.8	1.0
52/48	23.4	11.9	11.5	23.3	10.7	12.6
R_{on} (k Ω)	2-3-0.5			2-5-0.5		
	$V_{\text{gs}} = -1.5\text{ V}$	$V_{\text{gs}} = 0\text{ V}$	Difference	$V_{\text{gs}} = -1.5\text{ V}$	$V_{\text{gs}} = 0\text{ V}$	Difference
80/20	20.7	16.1	4.6	16.2	12.7	3.5

As described in Chapter 5.3, σ_{PZT} should be negative and correspond to P_{s} when $V_{\text{gs}} = -1.5\text{ V}$. When V_{gs} is increased to 0 V, σ_{PZT} should be still be negative and correspond to P_{r} . Therefore, a larger difference between P_{s} and P_{r} corresponds to a larger difference between σ_{PZT} when $V_{\text{gs}} = -1.5\text{ V}$ and σ_{PZT} when $V_{\text{gs}} = 0\text{ V}$. According to the simulation results in Chapter 4.3 and Chapter 4.4, σ_{PZT} is proportional to $n_{2\text{d}}$ which governs R_{on} . Consequently, a larger difference between P_{s} and P_{r} results in a larger decrease of R_{on} when V_{gs} is increased from -1.5 V to 0 V. Fig. 2.7 (d) suggests $P_{\text{r}}/P_{\text{s}}(52/48) < P_{\text{r}}/P_{\text{s}}(80/20) < P_{\text{r}}/P_{\text{s}}(20/80)$. Together with Fig. 2.7 (a) and Fig. 2.7 (b), it can be calculated that $P_{\text{s}} - P_{\text{r}}(52/48) > P_{\text{s}} - P_{\text{r}}(80/20) > P_{\text{s}} - P_{\text{r}}(20/80)$, which is in agreement with the trend of $\Delta R_{\text{on}}(52/48) \gg \Delta R_{\text{on}}(80/20) > \Delta R_{\text{on}}(20/80)$.

A comparison of the extent of CLM effect, gate leakage, and V_{th} is summarized in Table 5-4. The compared devices are “20/80 2-3-1”, “52/48 2-3-1”, and “80/20 2-3-0.5”. Table 5-4 suggests that the device with the Zr/Ti ratio of 52/48 has the severest CLM effect, the largest gate leakage in both $I_d - V_{ds}$ and $I_d - V_{gs}$ characteristics. Furthermore, it also exhibits the largest difference of V_{th} between the two sweep directions, which could be caused by the PZT polarization.

Table 5-4 Comparison of the CLM effect, gate leakage, and V_{th} of three devices.

	Extent of CLM effect	Magnitude of I_g in $I_g - V_{ds}$ curve when $V_{ds} = 6V$	V_{th} (first half)	V_{th} (second half)	Magnitude of I_g in $I_g - V_{gs}$ curve when $V_{gs} < V_{th}$
20/80 2-3-1	Low	10^{-6} mA	-2.7 V	-2.7 V	10^{-6} mA
52/48 2-3-1	High	10^{-2} mA	-3.3 V	-2.5 V	$10^{-2} \sim 10^{-1}$ mA
80/20 2-3-0.5	Medium	10^{-5} mA	-2.3 V	-2.7 V	$10^{-6} \sim 10^{-5}$ mA

6 Conclusions and recommendations

6.1 Conclusions

Novel PZT-on-GaN HEMTs were investigated in this work. Through literature study, it has been found that the polarization of PZT in the vertical direction differs from that in the lateral direction, which implies that PZT is strongly anisotropic. PZT thin films with 0.52 Zr composition have been reported to have the largest P_r and P_s , as well as the largest difference between the two values.

The devices were simulated using Silvaco TCAD. The simulation result of band diagram suggests that a PZT polarization which is parallel to the AlGaN spontaneous polarization can shift down the conduction band energy near the AlGaN/GaN interface, thus increase the 2DEG density. Furthermore, it has been found that n_{2d} scales linearly with σ_{PZT} , which in turn tunes R_{on} and V_{th} . Through the simulation of breakdown voltage, BV was observed to increase with the permittivity of PZT (dielectric RESURF) when it was regarded as an insulator, due to a flatter lateral electric field distribution caused by a higher $\epsilon_{r,PZT}$. While BV remained almost the same (semi-insulating RESURF) when PZT was regarded as a semiconductor.

PZT has been confirmed to be conducting by $I - V$ measurements. A deviation was observed between the two $I_d - V_{ds}$ curves within a dual sweep, which could be related to the flip of the horizontal polarization of PZT. By comparing the difference of R_{on} between $V_{gs} = -1.5$ V and $V_{gs} = 0$ V, it has been found that ΔR_{on} was the largest for 0.52 Zr composition, which can be explained by its largest difference between P_r and P_s .

A typical Schottky barrier diode characteristics was observed from $I_g - V_{gs}$ curves. The devices with 0.52 Zr composition exhibited the highest gate leakage and strongest CLM effect, while the devices with 0.2 Zr composition showed the lowest gate leakage and weakest CLM

effect. A hypothetical “hole induced gate leakage model” has been proposed to explain the substantial gate leakage below the threshold voltage for 0.52 Zr composition. The deviation between the two $I_d - V_{gs}$ curves within a dual sweep was observed in most devices, which could be linked to the different PZT polarization in the two sweep directions. A multi-peak $g_m - V_{gs}$ behavior has been observed in most devices.

The gate-drain breakdown voltages have been measured, which ranged from 330 V to 483 V. The BV/L_{gd} ratios were comparable to, or even better than those from literature. A two-step breakdown and a poor scaling of BV with L_{gd} were observed in $I_{dg} - V_{dg}$ curves. More dedicated test structures are needed to have a better result and analysis. To further investigate whether the PZT layer can increase the BV of the device, a reference device without PZT is necessary.

6.2 Recommendations

It is recommended that the reference devices without PZT should be fabricated in the future research, in order to have a direct comparison. Besides, it is unknown whether the PZT layer can breakdown. Therefore, the breakdown voltage of the PZT layer in both lateral and vertical direction should be measured with dedicated test structures. Further, the vertical polarization parameters of the PZT layer should be measured with special test structures, which can be used for analysis. To have a better result of R_{on} , contact resistance of the devices should be measured with dedicated test structures and then deducted from the total resistance. To have a better result of BV , it is recommended that the rectangular mask layout should be replaced by those with a cylinder shape to avoid the possible poor edge termination. The samples investigated in this report were fabricated in 2016, thus degradation could occur. Therefore, the preparation of the samples should be arranged close to the time when measurements are planned. Finally, considering the

fact that wire bonding is fragile, it should be avoided if possible. A recommendation is to add metal interconnections on the chip during fabrication, which extend to the edge and can be easily connected to a customized PCB.

References

- [1] Yole Développement, Status of the Power Electronics Industry (Villeurbanne, France, 2012).
- [2] Iacopi, F., Van Hove, M., Charles, M., & Endo, K. (2015). Power electronics with wide bandgap materials: Toward greener, more efficient technologies. *MRS Bulletin*, 40(5), 390-395.
- [3] Elibol, K., Nguyen, M. D., Hueting, R. J. E., Gravesteijn, D. J., Koster, G., & Rijnders, G. (2015). Integration of epitaxial Pb (Zr_{0.52}Ti_{0.48})O₃ films on GaN/AlGaN/GaN/Si (111) substrates using rutile TiO₂ buffer layers. *Thin solid films*, 591, 66-71.
- [4] Li, L., Liao, Z., Gauquelin, N., Nguyen, M. D., Hueting, R. J., Gravesteijn, D. J., ... & Koster, G. (2018). Epitaxial Stress - Free Growth of High Crystallinity Ferroelectric PbZr_{0.52}Ti_{0.48}O₃ on GaN/AlGaN/Si (111) Substrate. *Advanced materials interfaces*, 5(2), 1700921.
- [5] T. Mimura, S. Hiyamizu, T. Fujii, and K. Nanbu, "A new field-effect transistor with selectively doped GaAs/n-AlGaAs heterojunctions," *Jpn. J. Appl. Phys.*, vol. 19, no. 5, pp. L225-L227, May 1980.
- [6] Wang, R. (2008). Enhancement/depletion-mode HEMT technology for III-nitride mixed-signal and RF applications. Hong Kong University of Science and Technology (Hong Kong).
- [7] B.J. Baliga, *Fundamentals of Power Semiconductor Devices* (New York: Springer, 2008), pp. 23–86.
- [8] B.J. Baliga, *Fundamentals of Power Semiconductor Devices* (New York: Springer, 2008), pp. 92–100.

- [9] J. L. Hudgins, G. S. Simin, E. Santi, and M. Asifkhan, "An Assessment of Wide Bandgap Semiconductors for Power Devices", IEEE Trans. Power Electronics, vol. 18, pp. 907-914, 2003.
- [10] B.J. Baliga, Semicond. Sci. Technol. 28, 074011 (2013).
- [11] Chow, T.P, Ghezzi. SiC power devices. in III-Nitride, SiC, and Diamond Materials for Electronic Devices. Eds. Gaskill D.K, Brandt C.D. and Nemanich R.J., Material Research Society Symposium Proceedings, Pittsburgh, PA. 423 (1996), 69-73.
- [12] Ambacher, O., Smart, J., Shealy, J. R., Weimann, N. G., Chu, K., Murphy, M., ... & Stutzmann, M. (1999). Two-dimensional electron gases induced by spontaneous and piezoelectric polarization charges in N-and Ga-face AlGa_N/Ga_N heterostructures. Journal of applied physics, 85(6), 3222-3233.
- [13] F. Bernardini, V. Fiorentini, and D. Vanderbilt, Phys. Rev. B 56, 10024 (1997).
- [14] Yu, E. T., Dang, X. Z., Asbeck, P. M., Lau, S. S., & Sullivan, G. J. (1999). Spontaneous and piezoelectric polarization effects in III–V nitride heterostructures. Journal of Vacuum Science & Technology B: Microelectronics and Nanometer Structures Processing, Measurement, and Phenomena, 17(4), 1742-1749.
- [15] P. M. Asbeck, E. T. Yu, S. S. Lau, G. J. Sullivan, J. Van Hove, and J. M. Redwing, Electron. Lett. 33, 1230 (1997).
- [16] Xiao-Guang, H., De-Gang, Z., & De-Sheng, J. (2015). Formation of two-dimensional electron gas at AlGa_N/Ga_N heterostructure and the derivation of its sheet density expression. Chinese Physics B, 24(6), 067301.

- [17] Jena, D. (2008). Polarization effects on low-field transport & mobility in III-V nitride HEMTs. In Polarization effects in semiconductors (pp. 161-216). Springer, Boston, MA.
- [18] Lenka, T. R., & Panda, A. K. (2011). Characteristics study of 2DEG transport properties of AlGaIn/GaN and AlGaAs/GaAs-based HEMT. *Semiconductors*, 45(5), 650-656.
- [19] Pinin. (2010). Perovskite structure of PZT. Retrieved from <https://commons.wikimedia.org/wiki/File:Perovskite.svg>. Public domain.
- [20] Lee, E. G., Lee, J. K., Kim, J. Y., Lee, J. G., Jang, H. M., & Kim, S. J. (1999). Zr/Ti ratio dependence of the deformation in the hysteresis loop of Pb (Zr, Ti) O₃ thin films. *Journal of materials science letters*, 18(24), 2025-2028.
- [21] Izyumskaya, N., Alivov, Y. I., Cho, S. J., Morkoç, H., Lee, H., & Kang, Y. S. (2007). Processing, structure, properties, and applications of PZT thin films. *Critical Reviews in Solid State and Materials Sciences*, 32(3-4), 111-202.
- [22] B. Jaffe, W. R. Cook, Jr., and H. Jaffe, *Piezoelectric Ceramics*, Academic Press, London, 131 (1971).
- [23] Oikawa, T., Aratani, M., Funakubo, H., Saito, K., & Mizuhira, M. (2004). Composition and orientation dependence of electrical properties of epitaxial Pb (Zr x Ti 1– x) O₃ thin films grown using metalorganic chemical vapor deposition. *Journal of applied physics*, 95(6), 3111-3115.
- [24] Pintilie, L., Lisca, M., & Alexe, M. (2006). Epitaxial-quality PZT: insulator or semiconductor?. *Journal of optoelectronics and advanced materials*, 8(1), 7.
- [25] David R. Lide. (2005). *CRC Handbook of Chemistry and Physics*, version 2005.

- [26] Karmalkar, S., & Mishra, U. K. (2001). Very high voltage AlGa_N/Ga_N high electron mobility transistors using a field plate deposited on a stepped insulator. *Solid-State Electronics*, 45(9), 1645-1652.
- [27] Scott, J. F., Watanabe, K., Hartmann, A. J., & Lamb, R. N. (1999). Device models for PZT/Pt, BST/Pt, SBT/Pt, and SBT/Bi ferroelectric memories. *Ferroelectrics*, 225(1), 83-90.
- [28] Pintilie, L., Vrejoiu, I., Hesse, D., LeRhun, G., & Alexe, M. (2007). Ferroelectric polarization-leakage current relation in high quality epitaxial Pb (Zr, Ti) O₃ films. *Physical Review B*, 75(10), 104103.
- [29] Cai, Y., Zhou, Y., Lau, K. M., & Chen, K. J. (2006). Control of threshold voltage of AlGa_N/Ga_N HEMTs by fluoride-based plasma treatment: From depletion mode to enhancement mode. *IEEE transactions on electron devices*, 53(9), 2207-2215.
- [30] Ortiz-Conde, A., Sánchez, F. G., Liou, J. J., Cerdeira, A., Estrada, M., & Yue, Y. (2002). A review of recent MOSFET threshold voltage extraction methods. *Microelectronics Reliability*, 42(4-5), 583-596.
- [31] Sze, S. M., & Ng, K. K. (2006). *Physics of semiconductor devices*. John wiley & sons.
- [32] Chung, J. W., Roberts, J. C., Piner, E. L., & Palacios, T. (2008). Effect of gate leakage in the subthreshold characteristics of AlGa_N/Ga_N HEMTs. *IEEE Electron Device Letters*, 29(11), 1196-1198.
- [33] Lu, W., Yang, J., Khan, M. A., & Adesida, I. (2001). AlGa_N/Ga_N HEMTs on SiC with over 100 GHz $f_{sub T}$ and low microwave noise. *IEEE Transactions on Electron Devices*, 48(3), 581-585.

- [34] Zhang, N. Q., Keller, S., Parish, G., Heikman, S., DenBaars, S. P., & Mishra, U. K. (2000). High breakdown GaN HEMT with overlapping gate structure. *IEEE Electron Device Letters*, 21(9), 421-423.
- [35] Zhou, J., Huang, C. F., & Chen, Y. H. (2015). Theoretical analysis of dielectric modulated drift region for Si power devices. *IEEE Electron Device Letters*, 36(4), 378-380.
- [36] Van Dalen, R., Rochefort, C., & Hurkx, G. A. M. (2001). Breaking the Silicon limit using semi-insulating Resurf layers. In *Power Semiconductor Devices and ICs, 2001. ISPSD'01. Proceedings of the 13th International Symposium on* (pp. 391-394). IEEE.
- [37] Osenbach, J. W., & Knolle, W. R. (1990). Semi-insulating silicon nitride (Si₃N₄) as a resistive field shield. *IEEE Transactions on Electron Devices*, 37(6), 1522-1528.
- [38] Khandelwal, S., & Fjeldly, T. A. (2012, June). A physics based compact model for drain current in AlGaIn/GaN HEMT devices. In *Power Semiconductor Devices and ICs (ISPSD), 2012 24th International Symposium on* (pp. 241-244). IEEE.
- [39] Sque, S. (2013). High-voltage GaN-HEMT devices, simulation and modelling. *NXP Semiconductors*, Sep, 16.
- [40] Scott, J. F., Watanabe, K., Hartmann, A. J., & Lamb, R. N. (1999). Device models for PZT/Pt, BST/Pt, SBT/Pt, and SBT/Bi ferroelectric memories. *Ferroelectrics*, 225(1), 83-90.
- [41] Pintilie, L., Vrejoiu, I., Hesse, D., LeRhun, G., & Alexe, M. (2007). Ferroelectric polarization-leakage current relation in high quality epitaxial Pb (Zr, Ti) O₃ films. *Physical Review B*, 75(10), 104103.
- [42] Lu, B., Piner, E. L., & Palacios, T. (2010, June). Breakdown mechanism in AlGaIn/GaN HEMTs on Si substrate. In *Device Research Conference (DRC), 2010* (pp. 193-194). IEEE.

[43] Selvaraj, S. L., Watanabe, A., Wakejima, A., & Egawa, T. (2012). 1.4-kV breakdown voltage for AlGa_N/Ga_N high-electron-mobility transistors on silicon substrate. *IEEE Electron Device Letters*, 33(10), 1375-1377.

[44] Rowena, I. B., Selvaraj, S. L., & Egawa, T. (2011). Buffer thickness contribution to suppress vertical leakage current with high breakdown field (2.3 MV/cm) for Ga_N on Si. *IEEE Electron Device Letters*, 32(11), 1534-1536.

Appendix

Deckbuild simulation input

go atlas

AlGaN/GaN HEMT with tAlGaN=20nm, tGaN=1500nm, tPZT=100nm, Lgd=3 micron
set tPZT=0.1

set gdspace=3

pz refers to the net polarization charge at AlGaN/GaN interface

set pz=1.05e13

pzPZT refers to the PZT polarization charge at bottom surface of PZT

set pzPZT=0.4e13

set meshratio=0.5

mesh space.mult=1.0 width=30

Define mesh in horizontal direction

x.mesh loc=0.00 spac=0.2

x.mesh loc=1.00 spac=0.1

x.mesh loc=3.00 spac=0.1

x.mesh loc=5.00 spac=0.1

x.mesh loc=5+\$gdspace spac=0.1

x.mesh loc=6+\$gdspace spac=0.2

Define mesh in vertical direction

y.mesh loc=-1*\$tPZT spac=0.01/\$meshratio

y.mesh loc=0 spac=0.002/\$meshratio

y.mesh loc=0.02 spac=0.0002/\$meshratio

y.mesh loc=1.52 spac=0.5/\$meshratio

y.mesh loc=1.62 spac=0.004/\$meshratio

y.mesh loc=3.0 spac=0.15/\$meshratio

region num=1 material=algan y.min=0 y.max=0.020 x.comp=0.2

region num=2 material=gan y.min=0.020 y.max=1.52 substrate

region num=3 material=oxide y.min=1.52

region num=4 material=germanium y.min=-1*\$tPZT y.max=0

Define electrodes

electr name=gate x.min=3 x.max=5 y.min=-1*\$tPZT y.max=-1*\$tPZT

electr name=source x.min=0 x.max=1 y.min=-1*\$tPZT y.max=0.1

electr name=drain x.min=5+\$gdspace x.max=6+\$gdspace y.min=-1*\$tPZT y.max=0.1

electr name=substrate bottom

interface charge=\$pzPZT s.s y.min=0 y.max=0 x.min=3 x.max=5

interface charge=\$pz s.s y.min=0.02 y.max=0.02

```

models print srh fermi incomplete

# Adjust material parameters
material material=gan affinity=4.31 mun0=20 eg300=3.4 NC300=1.07e18 nv300=1.16e19 \
  mup0=10 vsatn=1.9e7 align=0.8 permittivity=9.5
material material=algaln affinity=3.82 mun0=10 eg300=3.96 NC300=2.07e18 nv300=1.16e19 \
  mup0=10 vsatn=1.1e7 align=0.8 permittivity=9.5

material material=germanium eg300=3.3 mun0=25 mup0=25 affinity=3.5 permittivity=600
NC300=1.4e20 NV300=3.4e20

impact selb material=gan

# Adjust workfunction gate
contact name=gate workfunction=5
contact name=source workfunction=4.2
contact name=drain workfunction=4.2

# Variables which should be plotted in case of TonyPlot
output con.band val.band band.param flowlines charge traps \
  e.mob h.mob e.vel ex.vel ey.vel h.vel hx.vel hy.vel qss polar.charge

# Start calculations
method gummel newton gum.init=5 single carriers=0 autonr
solve init
save outfile=HEMT_initial.str
tonyplot HEMT_initial.str

#####
# Calculation of I-V curves, omitted here #
#####

quit

```